



ADVANCED MASTERS IN STRUCTURAL ANALYSIS  
OF MONUMENTS AND HISTORICAL CONSTRUCTIONS



# Master's Thesis

Jonathan Knudtsen

Comparison of Modelling  
Approaches to Analysis of  
Masonry Arch Bridges

This Masters Course has been funded with support from the European Commission. This publication reflects the views only of the author, and the Commission cannot be held responsible for any use which may be made of the information contained therein.



## MASTER'S THESIS PROPOSAL

study programme: Civil Engineering  
study branch: Advanced Masters in Structural Analysis of Monuments and Historical Constructions  
academic year: 2016/2017


Student's name and surname: Jonathan Knudtsen  
Department: Department of Mechanics  
Thesis supervisor: Dr. Petr Kabele  
Thesis title: Comparison of Modelling Approaches to Analysis of Masonry Arch Bridges  
Thesis title in English: see above


Framework content: This thesis critically compares various masonry arch analysis techniques, evaluating the results from the point of view of structural response, modelling efficiency, and uncertainty in the input parameters. The techniques considered including limit analysis by hand, rigid-block analysis, and finite element analyses using a smeared crack model and a discrete crack model.

Assignment date: 7/04/2017 Submission date: 06/07/2017

If the student fails to submit the Master's thesis on time, they are obliged to justify this fact in advance in writing, if this request (submitted through the Student Registrar) is granted by the Dean, the Dean will assign the student a substitute date for holding the final graduation examination (2 attempts for FGE remain). If this fact is not appropriately excused or if the request is not granted by the Dean, the Dean will assign the student a date for retaking the final graduation examination, FGE can be retaken only once. (Study and Examination Code, Art 22, Par 3, 4.)

*The student takes notice of the obligation of working out the Master's thesis on their own, without any outside help, except for consultation. The list of references, other sources and names of consultants must be included in the Master's thesis.*

  
.....  
Master's thesis supervisor

  
.....  
Head of department

Date of Master's thesis proposal take over: July 2017  
  
.....  
Student

This form must be completed in 3 copies – 1x department, 1x student, 1x Student Registrar (sent by department)

## DECLARATION

Name: Jonathan Knudtsen

Email: jaknudtsen@gmail.com

Title of the Msc Dissertation: Comparison of Modelling Approaches to Analysis of Masonry Arch Bridges

Supervisor(s): Prof. Ing. Petr Kabele, Ph.D. and David Biggs, P.E., S.E., Dist.M.ASCE, HTMS

Year: 2017

I hereby declare that all information in this document has been obtained and presented in accordance with academic rules and ethical conduct. I also declare that, as required by these rules and conduct, I have fully cited and referenced all material and results that are not original to this work.

I hereby declare that the MSc Consortium responsible for the Advanced Masters in Structural Analysis of Monuments and Historical Constructions is allowed to store and make available electronically the present MSc Dissertation.

University: Czech Technical University

Date: July 5, 2017

Signature:



---

## ACKNOWLEDGEMENTS

I would like to first thank my supervisors, Prof. Petr Kabele and David Biggs, for their support and guidance in developing the work presented in this thesis. Their enthusiasm and availability during the past few months have been invaluable in bringing this work to a successful conclusion.

A special thank you goes to the European commission, whose support in the form of an Erasmus+ scholarship has made my participation in the SAHC program possible.

I would also like to acknowledge all the professors who taught during the first part of this course at the University of Padova. Their knowledge of structural analysis and preservation is inspiring, and formed the groundwork that allowed me to undertake this thesis.

The SAHC secretariat, in particular Ana Fonseca, have been very helpful in navigating the bureaucratic complexities of living in two foreign countries. Many thanks also to Elisa Trovo and Alexandra Kurfurstova for their support at the University of Padova and Czech Technical University respectively.

My deepest gratitude goes to my family and friends back home for their support and encouragement during this year abroad. Without your guidance and inspiration, none of this would have possible.

Finally, I want to acknowledge all my fellow SAHC students both in Padova and Prague. Your support and friendship have made this year fly by, and it has been a pleasure working with each and every one of you.

## **ABSTRACT**

Masonry arches have been used in bridge construction for millennia, and there are many masonry arch bridges still in service throughout the world. Despite masonry's wide use, it is only recently that scientific approaches to design and analysis have been developed. Lower-bound estimates of strength have been available since the 19<sup>th</sup> century, but these have largely been supplanted recently by rigid-block and finite element techniques developed over the last few decades. These modern analysis techniques provide better representation of arch structures, and are thought to provide more accurate results. However, their conservativeness and range of application are still being studied.

The purpose of this study is to critically compare various analysis techniques, evaluating the results from the point of view of structural response, modelling efficiency, and variations in the infill modelling. The techniques considered include limit analysis "by hand", rigid-block analysis, finite element analysis using a smeared crack model, and finite element analysis using a discrete crack model.

This study uses as a case study a 19<sup>th</sup>-century two-span stone masonry arch in Troy, NY, USA. In 1986, the bridge underwent a significant intervention in which the infill and spandrel walls were removed and replaced. At the time, the bridge was rated by idealizing the bridge as a series of elastic beams. The compressive stress and percent contact area were limited to allowable design values. A secondary purpose of the research was to compare the results of the elastic analysis with the results of the modern analyses, and to provide an updated load rating.

## **KEY WORDS:**

Masonry arch bridge, finite element, rigid block, analysis, modelling, comparison

## ABSTRAKT

Zděné klenby byly používány při výstavbě mostů po celá tisíciletí a dodnes je mnoho zděných klenbových mostů v provozu. I přesto, že používání zdiva je velmi rozšířené, vědecké přístupy k jeho navrhování a analýze byly vyvinuty jen v nedávné době. Odhady spodní hranice únosnosti jsou k dispozici již od 19. století, nicméně v posledních desetiletích byly tyto postupy do velké míry nahrazeny metodami diskrétních a konečných prvků. Tyto nové analytické techniky umožňují věrohodnější modelování klenbových konstrukcí, a proto se předpokládá, že poskytují přesnější výsledky. Nicméně, jejich konzervativnost a použitelnost jsou i dnes předmětem zkoumání.

Účelem této studie je kritické srovnání různých analytických metod, přičemž jsou porovnávány výsledné odezvy konstrukce, efektivita modelování a různé způsoby modelování násypu. Uvažované techniky zahrnují „ruční“ výpočet metodou mezní analýzy, metodu diskrétních tuhých prvků, metodu konečných prvků s rozetřenými trhlinami a metodu konečných prvků s diskrétními trhlinami.

Porovnání je provedeno na případové studii zděného klenbového mostu se dvěma oblouky z 19 století, který se nachází ve městě Troy, stát New York, USA. Na mostě byla v roce 1986 provedena rozsáhlá rekonstrukce, při které byly odstraněny a vyměněny poprsní zdi a násyp. V té době byl pro statické posouzení mostu použit elastický prutový model. Tlakové napětí a kontaktní plocha s vyloučením tahu v kritických průřezích byly omezeny na přípustné návrhové hodnoty. Druhým cílem prezentovaného výzkumu bylo porovnání výsledků pružné analýzy s výsledky moderních metod analýzy konstrukcí a aktualizace statického posouzení únosnosti mostu.

## KLÍČOVÁ SLOVA:

Zděné klenbové mosty, konečné prvky, diskrétní tuhé prvky, analýza, modelování, porovnání

## Table of Contents

1	Introduction .....	1
2	Background .....	3
2.1	Limit Analysis.....	3
2.2	Rigid-Block Analysis.....	4
2.3	Finite Element Method .....	4
2.4	Service Level Criteria .....	7
3	Case Study.....	9
3.1	History and Past Interventions .....	9
3.2	Previous Analyses.....	10
3.3	Bridge Geometry.....	10
3.4	Materials .....	11
3.4.1	Modelling Assumptions.....	12
3.4.2	Compressive Strength and Modulus of Elasticity .....	12
3.4.3	Tensile Properties .....	14
3.4.4	Infill Properties .....	15
3.4.5	Materials Summary .....	16
3.5	Loads.....	16
3.6	Effective Width.....	18
4	Limit Analysis .....	21
4.1	Graphic Statics Analysis .....	21
4.2	Kinematic Analysis.....	24
4.3	Comparison.....	26
5	Rigid Block Analysis .....	27
5.1	Modelling Assumptions .....	27
5.2	Results.....	29
6	FEM Modelling Assumptions .....	33
6.1	FEM Analysis with Smearred Crack Model .....	33
6.1.1	Geometry and Mesh .....	33
6.1.2	Materials .....	33
6.1.3	Loading and Boundary Conditions.....	36

6.1.4	Method and Parameters of Nonlinear Solution.....	38
6.2	FEM Analysis with Discrete Crack Model .....	39
6.2.1	Geometry and Mesh.....	39
6.2.2	Materials.....	40
6.2.3	Loading and Boundary Conditions .....	41
6.2.4	Cohesive Interfaces .....	43
6.2.5	Method and Parameters of Nonlinear Solution.....	45
7	Finite Element Analysis Results.....	47
7.1	Global Response.....	47
7.2	Crack Patterns and Deformation .....	48
7.3	Critical State Analysis .....	50
7.4	Comparison with Biggs and Rogers 1987 Analysis.....	56
7.5	Boussinesq Load Verification .....	57
8	Discussion.....	61
9	Conclusions.....	65
10	References.....	67



**List of Figures**

Figure 1 – Modelling strategies for masonry structures (Lourenço, 2010)..... 5

Figure 2 – Limit Analysis with middle third rule (Kidder, 1905) ..... 8

Figure 3 – Pawling Avenue bridge intervention, 1986..... 9

Figure 4 – Pawling Avenue bridge geometry ..... 11

Figure 5 – Characteristic masonry strength (ICE 2009)..... 13

Figure 6 – AASHTO tandem axle load ..... 17

Figure 7 – Truck load distribution through infill at arch crown ..... 19

Figure 8 – Graphic statics divisions and assumed hinge locations..... 22

Figure 9 – Graphic statics block force vectors ..... 22

Figure 10 – Graphic statics thrust line ..... 23

Figure 11 – Graphic statics load capacity..... 24

Figure 12 – Kinematic analysis divisions and loads ..... 25

Figure 13 – RING model ..... 28

Figure 14 –RING soil properties ..... 29

Figure 15 –RING arch failure mechanisms ..... 30

Figure 16 – ATENA mesh..... 33

Figure 17 – ATENA masonry constitutive relationships ..... 34

Figure 18 – ATENA compressive constitutive rule ..... 35

Figure 19 – ATENA crack opening law ..... 35

Figure 20 – ATENA Drucker Prager failure functions ..... 36

Figure 21 – ATENA materials, mesh, loading, and boundary conditions..... 38

Figure 22 – ATENA solution parameters..... 38

Figure 23 – ADINA surface distribution ..... 40

Figure 24 – ADINA mesh ..... 40

Figure 25 – ADINA hinge locations, TL loading, and boundary conditions ..... 41

Figure 26 – Boussinesq loading calculations ..... 42

Figure 27 – ADINA Boussinesq loading..... 43

Figure 28 – ADINA cohesive interface properties (base units kN and m)..... 44

Figure 29 – ADINA hinge location iteration..... 45

Figure 30 – ADINA solution parameters ..... 46

Figure 31 – FEM load-displacement plot .....	47
Figure 32 – ATENA-TL crack map with 20x deformation (LF = 13.2).....	49
Figure 33 – ADINA-TL crack opening with 20x deformation (LF = 13.5) .....	49
Figure 34 – ADINA-BSQ crack opening with 20x deformation (LF = 21.8) .....	50
Figure 35 – ATENA-TL at 67% compression (LF 3.2).....	52
Figure 36 – ADINA-TL at 67% compression (LF = 3.6).....	52
Figure 37 – ADINA-BSQ at 67% compression (LF = 4.0) .....	52
Figure 38 – ATENA-TL fourth hinge initiation (LF = 5.8).....	53
Figure 39 – ADINA-TL at fourth hinge initiation (LF = 7.6) .....	53
Figure 40 – ADINA-BSQ at fourth hinge initiation (LF = 9.6).....	53
Figure 41 – ATENA at first compressive plastic strain (LF = 9.4) .....	55
Figure 42 – ADINA-TL at first compressive plastic strain (LF = 8.8).....	55
Figure 43 – ADINA-BSQ at first compressive plastic strain (LF = 10.8).....	55
Figure 44 – ADINA-TL measured vertical stress along arch extrados.....	57
Figure 45 – Boussinesq vs ADINA loading at LF 2.1 .....	59
Figure 46 – Boussinesq vs ADINA loading at LF 8.25 .....	59
Figure 47 – Boussinesq vs ADINA loading at LF 13.5 .....	59

## List of Tables

Table 1: Masonry compressive strength in literature.....	14
Table 2: Masonry modulus of elasticity in literature .....	14
Table 3: Masonry material properties .....	16
Table 4: Infill material properties .....	16
Table 5: Kinematic analysis summary .....	25
Table 6: RING load factor results .....	31
Table 7: FEM load factors at critical steps .....	51
Table 8: Load factor summary for all models.....	62
Table 9: Estimated time requirements .....	63

## 1 INTRODUCTION

Masonry is one of the oldest building materials utilized in construction. Historically, most significant bridges were built using masonry arches, and many of these bridges are still used today. Both rail and highway bridges are being subjected to increasingly higher loads and frequencies, and thus engineers must find ways to adequately rate the structures, and if necessary design interventions.

Despite the age of masonry arch bridges, scientific approaches to design and analysis developed only recently. In the Middle Ages, trial-and-error approaches allowed builders to develop approximate geometrical formulas relating span, arch thickness, and buttressing requirements. These rules were used to construct many of the oldest masonry arch bridges in Europe. In 1675, Robert Hooke became the first to relate the thrust of an arch to an inverted catenary line, beginning the scientific inquiry into the analysis of arch structures. It was not until 1866, however, that the first formal graphic statics analysis technique was developed (Block, 2006). The graphic statics approach was used in designing many of the bridges built in Europe and the United States in the late 19<sup>th</sup> century and early 20<sup>th</sup> century. During the mid-20<sup>th</sup> century, the development of analysis techniques based on elasticity almost entirely supplanted the use of graphical means of analysis (Block, 2006).

Heyman (1982) developed the lower-bound (or safe) theorem based on the graphic statics approach above. Heyman's contribution was the recognition that an arch structure can be considered safe if any statically admissible state of equilibrium can be found. This led to a new interest in limit analysis techniques for masonry arches. At the same time, modern computational power was also beginning to allow for more detailed analyses. Two basic analyses types emerged: Those based on rigid blocks forming hinges and kinematic mechanisms, and more detailed analyses based on the finite element method (FEM). Within these two approaches, there exist large variations in the assumptions and level of detail required.

The goal of this project was to compare the results of various analysis techniques applied to a simple two-span masonry arch bridge. The following analysis techniques were used:

- Limit analysis, using the graphic statics (lower bound) and kinematic (upper bound) approaches.
- Rigid-block method of analysis using the LimitState:RING (RING) software.
- FEM smeared crack modelling using ATENA software.
- FEM discrete crack modelling using ADINA software.

For each technique, the load factor causing collapse was calculated. By comparing these values with the degree of effort and computational power required, the efficiency of each technique can be estimated.

A secondary objective of this study was to provide an updated load rating for the bridge used in the case study. Biggs and Rogers (1987) did an elastic analysis of the structure based on allowable stress design, utilizing a service-level criterion requiring a minimum 67% contact area at the critical section. As service level criteria are still poorly defined for masonry arch bridges, differing approaches are analyzed and discussed.

## 2 BACKGROUND

The basic theories, applications, and limitations of each analysis technique used in this study are described below. Additionally, the development of service level criteria is also reviewed.

### 2.1 Limit Analysis

The simplest method of arch analysis is the limit analysis, incorporating graphic statics as a lower bound, and kinematic analysis as an upper bound. These methods give the collapse load only, and do not provide information on displacement or intermediate loading conditions. Additionally, these methods require the user to specify the locations of both the loads and the hinges, which can be problematic when considering the moving loads on a bridge. However, they are very simple to implement, and they give conservative results.

The limit analysis method requires three basic assumptions:

- Masonry has null tensile strength.
- The compressive strength is infinite.
- No sliding takes place between units.

If these conditions are met, the theorems of limit analysis apply. The lower bound theorem states that if a statically admissible state of equilibrium can be found, the structure is safe. This is demonstrated using the thrust line drawn using graphic statics. The upper bound theorem states that if a kinematically admissible mechanism can be found, for which the work developed by external forces is positive or zero, the structure will collapse. This is demonstrated by calculating the force required to form kinematic mechanisms based on the loading and hinge locations. Finally, the uniqueness theorem states that a limit condition will be reached if both statically and kinematically admissible collapsing mechanisms can be found. In other words, by varying the assumed hinge and thrust line assumptions, a unique value can be found where the upper and lower bound methods will meet.

## 2.2 Rigid-Block Analysis

Rigid block analysis automates the principles of limit analysis described above, and allows for some improvements. Most importantly, the compressive strength can be limited, sliding can occur between blocks, and a more detailed infill model can be used. RING uses the rigid-block formulation with these specified improvements. The tensile strength is still assumed to be zero. Theoretically, these improvements could be applied to the hand-calculations as well, but the process would be highly iterative and complex. Instead of using a trial-and-error method, RING uses mathematical optimization techniques, the details of which can be found in the program documentation.

Like the limit analysis approach, the arch is divided into a finite number of voussoirs, with hinges limited to forming between the voussoirs. The equations of static equilibrium are applied to each voussoir. To test for ultimate collapse, the “yield” and “mechanism” conditions are used:

- Yield condition: This condition is met if the thrust line falls outside of the masonry arch. It can also be met through sliding, if the angle at which the thrust line crosses a joint is greater than  $\tan^{-1}(\mu)$ , where  $\mu$  is the coefficient of friction.
- Mechanism condition: The line of thrust must touch the edge of the arch or cross interfaces at angles greater than  $\tan^{-1}(\mu)$  at sufficient locations to transform the structure into a mechanism.

The load factor is increased, maintaining equilibrium, until both of these conditions have been met. This load is taken as the collapse load.

## 2.3 Finite Element Method

Masonry is a nonhomogenous, anisotropic composition of two different materials, the units and the mortar, which have very different mechanical properties. This presents a significant challenge when using the finite element method to model masonry structures. Lourenço (2010) describes three basic approaches to modelling masonry, illustrated in Figure 1. The first case shows detailed micromodelling, in which the mortar and the units are modelled independently, incorporating all the material properties of each material. Interface units allow for cracking and

slip between the units and mortar. In theory, this type of model can perfectly describe a masonry structure. However, it is extremely computationally expensive, and it is only as accurate as the material properties that are specified. These properties are often unknown, and can be difficult to determine accurately. The second case shows simplified micromodelling, in which the mortar is not represented as a continuum but is approximated by zero-thickness joints. The units are expanded to the midpoint of the mortar joints to preserve the geometry. This method is more computationally efficient than the first method, and it still allows for the consideration of individual units. However, some accuracy is lost due to the simplification of the joints, and it is still too computationally expensive to be used for most large-scale applications. Finally, there is the macro-modelling approach, in which the masonry is treated as a homogenous anisotropic or isotropic continuum (Lourenço, 1996). This method is commonly used for modelling entire masonry structures. Despite the major simplifications involved, this method can still deliver accurate solutions, provided the input parameters accurately represent the true material properties.

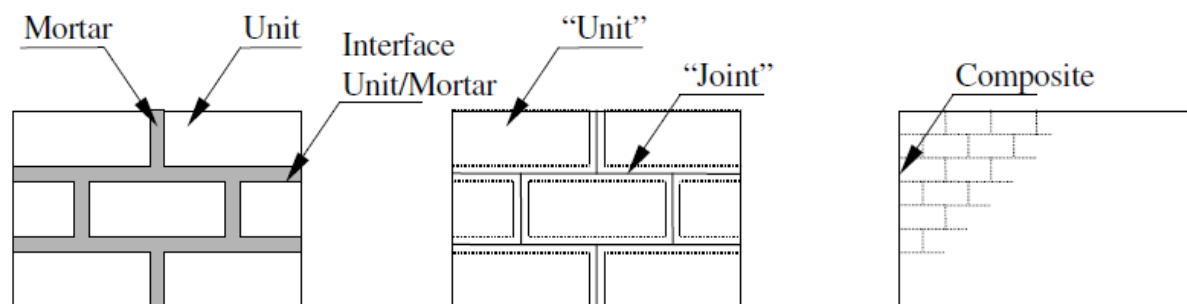


Figure 1 – Modelling strategies for masonry structures (Lourenço, 2010)

As the present study requires analyzing a full structure, the macro-modelling approach was used. Two different cracking models were used: A crack band model implemented in ATENA, and a discrete crack model implemented in ADINA.

The crack band model uses the smeared crack approach, in which cracking is represented as strain within elements. The strain is decomposed into elastic and cracking strain, shown below:

$$\varepsilon = \varepsilon_e + \varepsilon_{cr} \quad (2.1)$$

Without refinement, the smeared crack model suffers from pathological mesh sensitivity. For this reason, the crack band model assumes that the crack strain develops over a band of finite width. The stress corresponding to each strain is calculated separately using elastic and cracking constitutive rules respectively. Cracking is initiated when the maximum principal stress reaches the material tensile strength. After cracking, the constitutive law is given in terms of cohesive stress vs. crack opening displacement. The crack strain is calculated as the crack opening displacement divided by the cracking band width. The crack forms in the direction perpendicular to the maximum principal stress. In the present study, the fixed crack model was used, meaning the crack continues to propagate in its initial direction. Cracking is initially widespread, but the localized reductions in stiffness cause most of the deformation to accrue at large, identifiable cracks.

Discrete crack modelling, on the other hand, introduces cracks as actual discontinuities in displacement. Many different methods are used to model this, but one of the simplest is implemented in this study, since options were constrained by the capabilities of the modelling software used. In this method, the potential crack locations are defined by the user as interface lines. The preprocessor generates dual nodes along these lines and inserts linear zero-thickness elements. The constitutive law assigned to the interface elements relates the stress transferred between the adjacent elements to their relative displacement. The law is formulated in such a way that the relative displacement remains very small in compression and prior to failure in tension. After failure, a linear softening relationship is used, again relating stress to displacement.

The discontinuities in the displacement represented by the discrete crack model correspond to real phenomena, and thus the model can provide a good representation of cracking. However, in its simplest formulation, the locations where the cracks occur and propagate are constrained, detracting from the model's ability to represent reality. More detailed discrete cracking models have been developed, but these may require specialized software, and are often computationally expensive (Borst *et al.*, 2004).



The crack band modelling approach sacrifices some realism in representing the cracking as strain within elements, but it allows cracking to develop within any element. This eliminates the need for the user to specify crack locations, and reduces mesh sensitivity. Furthermore, this method simplifies the model since it does not require any discontinuities within the mesh. For these reasons, it is commonly used in FEM studies.

This study utilizes in compares both crack modelling approaches. For masonry arch structures, the most basic form of discrete crack modelling is more easily implemented than in concrete structures, since the approximate locations of the hinges can be identified a priori. Iterative analyses can be used to refine the locations of the hinges. The differences between the discrete and crack band models are discussed in greater detail in Borst *et al.* (2004).

## 2.4 Service Level Criteria

An arch structure fails when it develops a mechanism, requiring a minimum of four hinges. Hinges form where tensile cracking propagates through the depth of a section, leaving only a small band to carry compressive stress. This is the ultimate load condition, and should not be used for service-level loading. Various limits for service level loading have been developed, and they are reviewed in this section.

In the early 20<sup>th</sup> century, the fully elastic “rule of one third” was commonly used to analyze masonry bridge structures. Heyman (1982) credits its rigorous development to Pippard (1936), but the rule can be found as early as the 1905 Kidder handbook, illustrated in Figure 2. The rule required that the thrust line fall within the middle third of the arch cross section throughout the arch (in Figure 2, between points A and B). If the load is at the third point, the stress on the opposite outermost fiber is zero, meaning the first crack initiation is taken as the service limit for the assumption of null tensile strength.

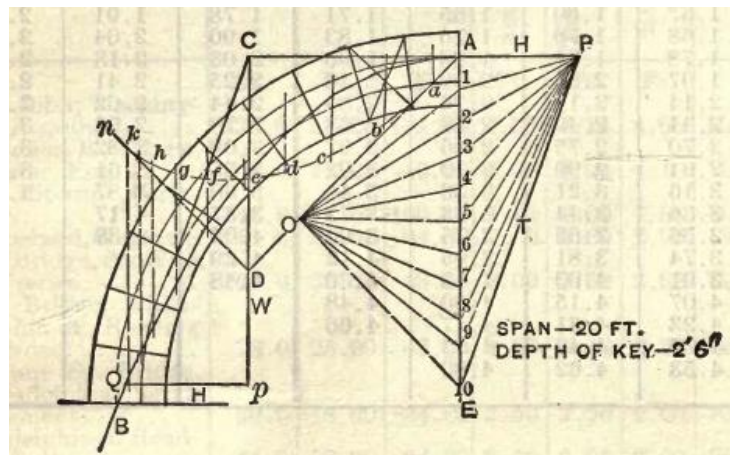


Figure 2 – Limit Analysis with middle third rule (Kidder, 1905)

This approach is extremely conservative, as (by definition) only one of the four hinges required for failure has even begun to initiate. Recognizing this, later approaches allowed for some cracks at service loads. Biggs and Rogers (1987) state that it is common to use a “rule of one half”, in which the thrust line is limited to acting in the middle half, meaning tensile stresses are allowed the bottom quarter of the arch. In their study, they use an approach in which tension is allowed in the bottom third of the arch.

Loo and Yang (1991) developed a finite element program to analyze masonry arches to address the perceived shortcomings of the previously described analysis methods. They do not, however, specify criteria for service level load-capacity ratings. As no further studies could be found, a new service level criteria is here proposed, corresponding to the first crack initiation of the fourth hinge. This limit is guaranteed to occur prior to arch failure, and it will be shown that it is appropriately conservative. For comparison, the load capacities using Biggs and Roger’s 67% contact area limit are also recorded.

### 3 CASE STUDY

The bridge modelled in this study is located in Troy, New York, USA. It is a double arch stone masonry bridge, built in approximately 1875. It underwent significant alterations in 1986, when a concrete box system was added to confine the fill. The following sections detail the history, materials, and geometry of the bridge.

#### 3.1 History and Past Interventions

The history of the bridge is documented in Biggs and Rogers (1987), the key elements of which are summarized below. The bridge spans the Poesten Kill just outside the city of Troy, and was built using dry-stacked limestone blocks, most likely from a nearby quarry. It originally carried at least one set of trolley tracks, and had cantilevered wooden sidewalks. The tracks were removed in the 1920s, and the sidewalks were removed in 1975. It currently carries three lanes of traffic. In the 1980s, New York state bridge inspectors noticed significant bulging and deterioration in the spandrel walls, prompting an intervention to restore and strengthen the bridge. The spandrel walls and infill were removed, and a concrete box system was installed to provide confinement to the infill. The stones of the spandrel walls were then used as an anchored veneer to cover the concrete walls. Pictures taken before and during this operation are shown in Figure 3.



Figure 3 – Pawling Avenue bridge intervention, 1986

### 3.2 Previous Analyses

Biggs and Rogers (1987) did an elastic analysis of the bridge using allowable stress design (ASD). A matrix analysis program was used to model the structure using a series of beam elements. Loading from a single AASHTO HS-20 truck was applied to the bridge, and the resulting compressive and tensile stresses were determined. The location of the load and the critical section are not specified, but it is assumed that the critical locations were selected. Since it was assumed that the blocks could not transfer tension, the calculated stress distribution was transformed into an equivalent compressive distribution. The minimum contact area required was taken as 67%, and the allowed compressive stress was 400 psi (2.76 MPa). The modulus of elasticity was taken as 6,000 ksi (41.4 GPa). For the most critical case studied, in which three hinges have formed, the resulting compressive stress was 326 psi (2.25 MPa), with a 75% contact area. Since these values met the specified criteria, the bridge was deemed sufficient for the applied load.

In the three decades since this report was published, there have been significant changes in the analysis procedures for arch structures. For all structures and materials, strength-based design procedures have largely replaced allowable stress design procedures. Since the strength of a masonry arch is more dependent on geometry than material properties, these design procedures are better suited to the analysis of arch structures.

A second, no less important development, has been the increasing recognition of the large difference between masonry unit strength and masonry prism (or wall) strength. In ASD design, this distinction could be blurred through the use of large reduction factors. The 1987 report gives only a single compressive strength value, without specifying the material it applies to. It is used as the strength of the masonry system, and since the value is quite small, it is conservative. But separating the safety factor from uncertainty factors gives a better representation of reality, and allows engineers to use higher load ratings if warranted.

### 3.3 Bridge Geometry

The bridge geometry parameters were determined from drawings made available from the 1986 intervention, and they are shown in Figure 4. The bridge is approximately 27.1 m long and 16.8

m wide. Sidewalks are present on both sides, so the roadway width is 12.4 m. The arch radius is 6.71 m (22 ft), with a subtended angle of 144 degrees. The thickness of the arch voussoirs is 61 cm (2 ft). The deck is located 2.42 m above the crown of the arch intrados. The infill is extended 5.2 m on each embankment, in order to allow for arch movement into the fill.

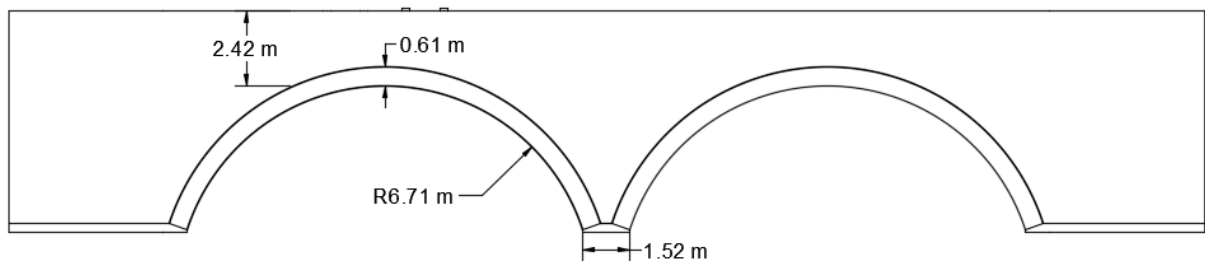


Figure 4 – Pawling Avenue bridge geometry

### 3.4 Materials

During the 1986 strengthening intervention, a state geologist confirmed that all of the stones appear to be limestone, likely of the Coeymans type found near South Bethlehem, N.Y. The Biggs and Rogers report states that the blocks appear to have been placed with dry joints, with a lime-based mortar used only where the stones were not in contact. In some cases, the joints were subsequently tuck-pointed.

No material tests were done on the bridge masonry, so material properties were estimated from existing literature. Biggs and Rogers (1987) reviewed allowable stresses listed in U.S. building codes from c. 1915, and report values between 2.96 MPa and 4.78 MPa (430 – 694 psi). Locally available limestone was rated at 3.96 MPa (575 psi). Note that these values are allowable stresses, and thus they have already been reduced from the measured material strength. These safety reduction factors could be quite large. As an example, the Kidder handbook (1905) recommends using a reduction factor of 20 for masonry arch bridges. Applying this factor to the limestone rated at 3.96 MPa gives a material strength of 79.2 MPa. Based simply on the order of magnitude, it follows that this corresponds to the strength of the limestone units, rather than the masonry system. The methods used to estimate the strength of the masonry system are described in the following section.

The density of the limestone was taken as  $27.5 \text{ kN/m}^3$ , as reported in Biggs and Rogers. The earth infill consists of well-compacted silty sand and gravel, and its density was taken as  $19 \text{ kN/m}^3$ .

For all of the finite element models, the plane strain assumption was used.

### 3.4.1 Modelling Assumptions

For macro-modelling approaches it is necessary to estimate the strength of the combined masonry unit-joint system, which is typically much weaker than the masonry units themselves. Eurocode 6 prescribes a formula for estimating this strength using the individual strengths of the masonry and mortar. In this case, however, this equation returns a value of zero strength since the units are dry-stacked, and there is no mortar. For this reason, the material properties were estimated from properties reported in the literature.

### 3.4.2 Compressive Strength and Modulus of Elasticity

Boothby and Fanning (2004) developed recommendations for masonry properties using frame-analysis techniques. In Boothby's original 2001 paper, he recommends compressive strength values ranging from 1 to 3 MPa, but in the 2004 paper, he updates these to range from 3 to 15 MPa. The modulus of elasticity ranges from 1 to 15 GPa. The recommendations were developed based on four sandstone and limestone masonry arch bridges in Ohio, U.S.A. Jaafar *et al.* (2006) did uniaxial compression tests on dry-stacked interlocking cementitious blocks. Individual blocks, prisms, and wall sections were tested. The wall compressive strength was found to be 39% of the unit strength. Magenes *et al.* (2010) did a series of uniaxial compression tests on roughly-worked sandstone prisms with lime-based mortar. The authors report an average maximum compressive strength of 3.28 MPa, and an average modulus of elasticity of 2.55 GPa. Atamturktur *et al.* (2016) tested dry-stacked CMU units in uniaxial compression. Both ground and unground samples were tested. The prism strength of the ground samples was found to be correlated with the strength of the units, and was estimated as 50%. The prism strength of the unground units, on the other hand, did not depend on the strength of the units, and varied between 8 and 13 MPa.

The Italian building code IMIT (2009) provides guidelines for estimating the material properties of masonry based on visual inspection. Borri *et al.* (2014) provide an English translation of this guide. For ashlar masonry, the code recommends a compressive strength of 6 – 8 MPa, and a modulus of elasticity of 2.4 – 3.2 GPa. For soft stone masonry, including limestone, the ranges are 1.4 – 2.4 MPa and 0.9 – 1.26 GPa respectively. The ICE Manual of Bridge Engineering (2009) provides the graph shown in Figure 5 to estimate the compressive strength of masonry. For the limestone used in the present study, the masonry strength would range between 5 and 10 MPa, depending on which curve is deemed most appropriate. The ICE code gives  $900 \cdot f_k$  as the modulus of elasticity.

The reported compressive strength and modulus of elasticity from each of the studies and codes are summarized in Tables 1 and 2. All of the compression strengths reported are mean strengths (denoted  $f_m$ ), with the exception of the ICE code, which reports characteristic strength (denoted  $f_k$ ). The strength of the masonry units themselves is denoted  $f_b$ .

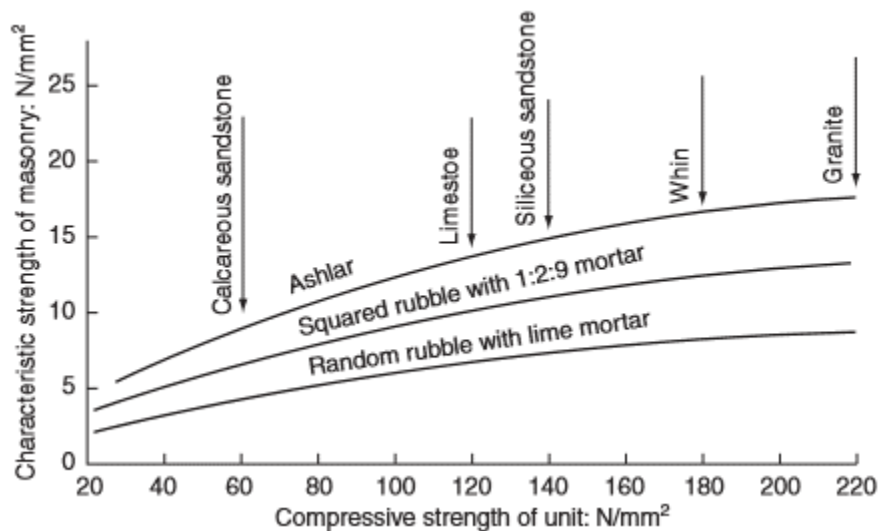


Figure 5 – Characteristic masonry strength (ICE 2009)

Table 1: Masonry compressive strength in literature

Author	Masonry type	$f_m$
Boothby and Hanning (2004)	Cut stone masonry, narrow joints with mortar	10-15 MPa
	Cut stone masonry, wide joints	5-10 MPa
	Rubble masonry, wide joints	3-5 MPa
Jaafar <i>et al.</i> (2006)	Hollow cementitious interlocking blocks, no mortar	39% * $f_b$
ICE (2009)	Stone masonry, ashlar or squared rubble	5-10 MPa
IMIT (2009)	Ashlar stone masonry	6 - 8 MPa
	Soft stone masonry (limestone)	1.4 - 2.4 MPa
Magenes <i>et al.</i> (2010)	2-leaf roughly cut sandstone wall with lime mortar	3.18 MPa
Atamturktur <i>et al.</i> (2016)	CMU, unground, no mortar	8-13 MPa
	CMU, ground, no mortar	50% * $f_b$

Table 2: Masonry modulus of elasticity in literature

Author	Masonry type	E
Boothby and Hanning (2004)	Cut stone masonry, narrow joints with mortar	5-15 GPa
	Cut stone masonry, wide joints	3-5 GPa
	Rubble masonry, wide joints	1-3 GPa
ICE (2009)	Thin jointed, coursed stone masonry	900 * $f_k$
IMIT (2009)	Ashlar stone masonry	2.4 - 3.2 GPa
	Soft stone masonry (limestone)	0.9 - 1.26 GPa
Magenes <i>et al.</i> (2010)	2-leaf roughly cut sandstone wall with lime mortar	2.55 GPa

From these studies, it was determined that a masonry strength between 5 and 10 MPa was a reasonable assumption. Thus 7.5 MPa was taken as the actual compressive strength. The modulus of elasticity was estimated using the ICE code multiplication factor of 900, giving a value of 6.75 GPa.

### 3.4.3 Tensile Properties

Because the units are dry-stacked, the tensile strength is almost non-existent. However, a nonzero value is necessary for modelling purposes. For this reason, the tensile strength was estimated as 2% of the compressive strength, giving a value of 0.15 MPa. Simplifying the fracture energy curve to a triangular shape, the fracture energy can be estimated as follows:

$$G_f = \frac{f_t d_u}{2} \quad (3.1)$$



For the ductility index  $d_u$ , Lourenço (2010) recommends values between 0.018 and 0.040 mm, based on the results of van der Pluijm (1999) and Lourenço *et al.* (2005). Both authors tested brick masonry. Vasconcelos (2005) did tests on granite, and found that the ductility index varied with tensile strength. Using Vasconcelos' equation, Lourenço (2010) reports that for an average granite tensile strength of 3.5 MPa, the ductility index would be 0.057 mm, or about twice the value found for brick masonry. For this study, Lourenço's approximation of 0.029 mm was adopted as the ductility index, giving a fracture energy of 2.175 N/m.

#### 3.4.4 Infill Properties

The strength of a masonry bridge is highly dependent on the properties of the earth infill. The infill plays three significant roles (RING, 2016):

- The dead weight of the soil pre-stresses the arch, delaying the formation of hinges.
- The infill serves to distribute loads over larger areas.
- The outward movement of arch voussoirs under a kinematic mechanism activates passive soil pressures in the horizontal direction.

For these reasons, the analysis is sensitive to changes in the soil properties. Unfortunately, the literature on this topic is limited, so assumptions must be made.

Cavicchi and Gambarotta (2007) provide perhaps the most thorough overview of the topic. The authors used an angle of friction of 37 degrees, based on the experimental results of Page (1987). The cohesion was reported as 12 kPa, based on calibrations with experimental results. Biggs and Rogers (1987) describe the infill in the bridge currently being studied as consisting of "silty sand and gravel" prior to the strengthening intervention. All of the infill was removed, but the construction documents specify that it should be replaced with "select structural fill." Because the fill appears to be of good quality, both before and after the intervention, the modelling assumptions of Cavicchi and Gambarotta were adopted for this study.

The modulus of elasticity was assumed to be 25 MPa, based on data available at the geotechnical information website GeotechData.info.

### 3.4.5 Materials Summary

The material properties used for both the infill and the masonry are summarized in the tables below. Poisson's ratio for masonry was taken as 0.2, while for the soil it was taken as 0.3. These values are typical for these materials.

Table 3: Masonry material properties

Compressive Strength (MPa)	7.5
Modulus of Elasticity (GPa)	6.75
Tensile Strength (MPa)	0.15
Fracture Energy (N/m)	2.175
Density (kN/m <sup>3</sup> )	27.5
Poisson's Ratio	0.2

Table 4: Infill material properties

Modulus of Elasticity (MPa)	25
Friction Angle (deg)	37
Cohesion (kPa)	12
Density (kN/m <sup>3</sup> )	19
Poisson's Ratio	0.3

Note that the masonry properties differ from those used for the 1986 report, which used a compressive strength of 2.76 MPa and a modulus of elasticity of 41.4 GPa. The low compressive strength is the result of using an already factored value, while the high modulus of elasticity represents only the stiffness of the masonry units, not the unit/joint system.

### 3.5 Loads

The bridge loading was taken in accordance with the AASHTO-LRFD standard. The code specifies that the governing load case shall be taken as the superposition of a lane load and either a truck or tandem axle load. All possible loading scenarios were run in the RING software, and it was determined that the governing load case is the combined lane load and truck tandem axle. However, the results in RING demonstrated that it is more conservative to run the tandem load alone, neglecting the lane load. Thus the lane load was ignored. The tandem

load consists of two axles spaced 1.22 m (4 ft.) apart, each carrying a load of 111.2 kN (25 kips). The tandem load is shown in Figure 6. The tire patch size is 254 mm long and 508 mm wide (10 in. x 20 in.). The transverse spacing between the truck tires is given as 1.83 m (6 ft.).

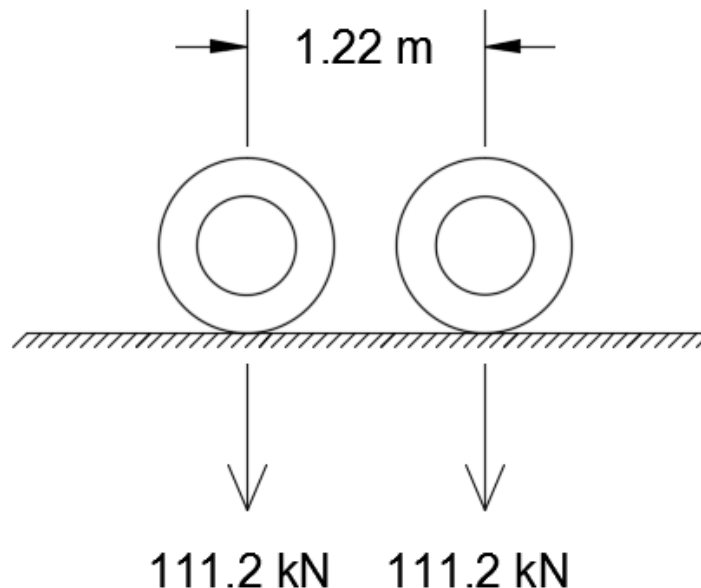


Figure 6 – AASHTO tandem axle load

The longitudinal placement of the load governs the type of hinge mechanism (5-hinge or 4-hinge) that forms, as well as load at which failure occurs. Audenaert *et al.* (2009) demonstrated that the 4-hinge arch, with the load off-center, is more critical than the 5-hinge arch, with the largest differences observed for relatively thick arch rings. With an arch thickness to radius ratio of 0.18, the authors report an 8.62% difference between the centered and off-center failure loads. The arch in the present study has a thickness to radius ratio of 0.09, and the RING model gives a 4.1% difference. Using RING, the location of the critical off-center load was found to be 1.28 m from the arch centerline. No difference was found between the side closer to the center pier and the side closer to the embankment. Varying the load location between 1.0 m and 1.5 m off-center resulted in changes in capacity of less than 1%, and thus the calculated value of 1.28 m off-center was used in all subsequent models.

### 3.6 Effective Width

Masonry arch bridges are three-dimensional structures, largely due to the effects of loading. The live loads are applied as concentrated loads, which are then dispersed through the earth infill. This means that neither the load distribution or the deformations are uniform in the transverse direction. However, for simplicity, it is often desirable to analyze these bridges using a two-dimensional model. This requires estimating the effective bridge width over which the load of a single lane should be spread.

Very little data could be found dealing with the subject of effect width. The RING User Manual introduces the subject by stating that “there is little real evidence on which to base rational rules.” For this reason, empirical approximations are generally used. Both AASHTO-LRFD and the RING User Manual recommend distributing the load through the fill using a 2:1 slope. The RING User Manual further specifies that the width calculated at the crown of the arch may be used for the entire bridge. The width may also be reduced depending on edge conditions, the presence of cracks, and overlapping distributions from multiple vehicles.

In the present study, no significant longitudinal cracks were reported (other than the spandrel wall separation prior to the intervention). Furthermore, the presence of sufficiently wide sidewalks on both sides of the bridge means that the effective width does not need to be reduced for edge conditions. The lane loads, however, may overlap, depending on the transverse location of the trucks on the bridge. Using Google’s satellite view (2017), it was determined that the width of the two outer lanes is 4.37 m, while the width of the inner lane is 3.67 m. The AASHTO-LRFD code specifies that the center of the truck tire be placed 2 ft. (0.61 m) from the edge of the design lane. This means that tire center-to-center distance between two trucks is 1.22 m, or approximately 0.71 m edge-to-edge. When spread at a 2:1 ratio, the loads overlap, giving a reduced effective width of 3.65 m. This is illustrated in Figure 7. In the interest of being conservative, this value was used throughout the study.

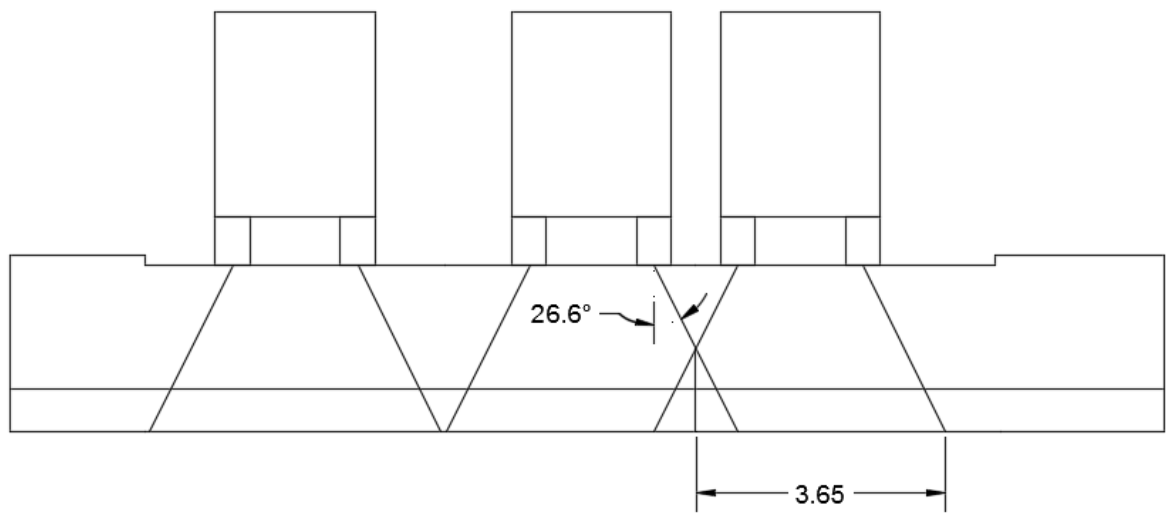


Figure 7 – Truck load distribution through infill at arch crown

This page intentionally left blank.

## 4 LIMIT ANALYSIS

The graphic statics and kinematic approaches were used to analyse the limit condition causing collapse. The biggest difference between this approach and subsequent modelling approaches arises in the modelling of the infill. In limit analysis, only the vertical weight of the infill is included, while the horizontal passive pressure and live load dispersion effects are neglected.

A further simplifying assumption was adopted for this study, in which the load was simplified to a single point load of 222.4 kN acting at midspan. Since both the arch and loading are symmetric in this case, the load causing collapse can be determined directly. Off-center loading requires time-intensive graphical iteration, in which the load must be assumed at the outset and then checked against the final results. This simplification is not recommended if limit analysis is the primary means of evaluation, since it will yield unconservative results. However, it can provide a first-order estimate of the load capacity of an arch when more intensive methods will be used later. The results of this analysis can be compared with the RING model that has the infill dispersion and passive pressure effects turned off. The details of this model are given in the Rigid Block Analysis section below.

### 4.1 Graphic Statics Analysis

The arch was divided into 16 equally spaced voussoirs, with the infill blocks directly above. Since the load is centered, five hinges are required for structural failure. The location of these hinges must be assumed, so as a first iteration, it was assumed that the hinges form in such a way that the arch is split into four equal parts. If the uniqueness theorem does not converge to an acceptable value, the location of the hinges must be adjusted. In this case, the assumptions made for the first iteration were sufficient to reach acceptable convergence. The arch divisions, loading, and hinges are shown in Figure 8, with the hinges marked in purple.

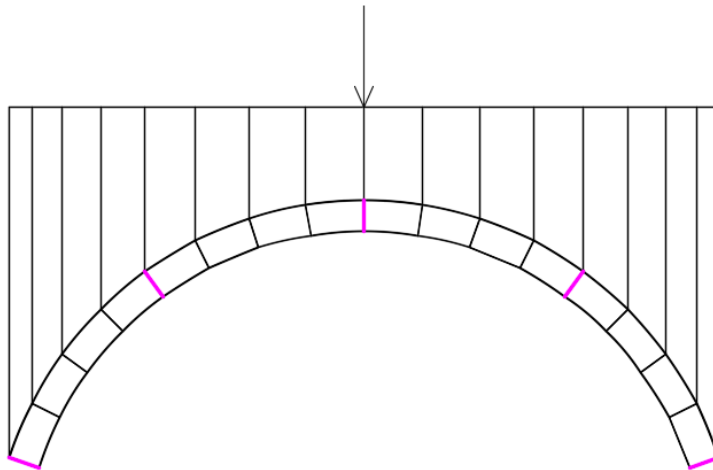


Figure 8 – Graphic statics divisions and assumed hinge locations

Since the arch and loading are symmetric, only the right side of the arch was analyzed, shown in Figure 9 below. The blue lines mark the weight and centroid of each block, using a scale factor of 73. The calculations were originally done using a bridge width of 1 m, and a scale factor of 20. Multiplying the force vectors by the bridge width of 3.65 m gives the scale factor of 73.

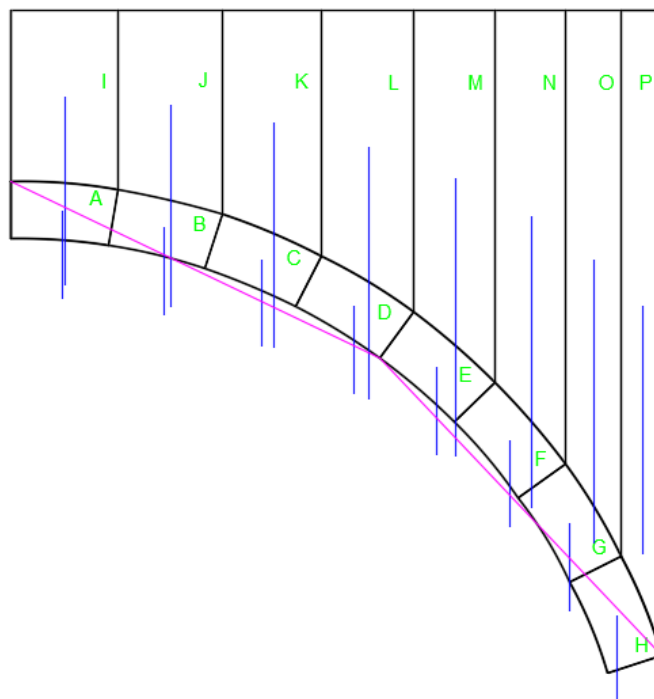


Figure 9 – Graphic statics block force vectors



The procedures for graphic statics were then followed to determine the critical load. These procedures are well documented elsewhere, and have been used since the early 20<sup>th</sup> century (Kidder, 1905). The resulting thrust line is shown in Figure 10 below.

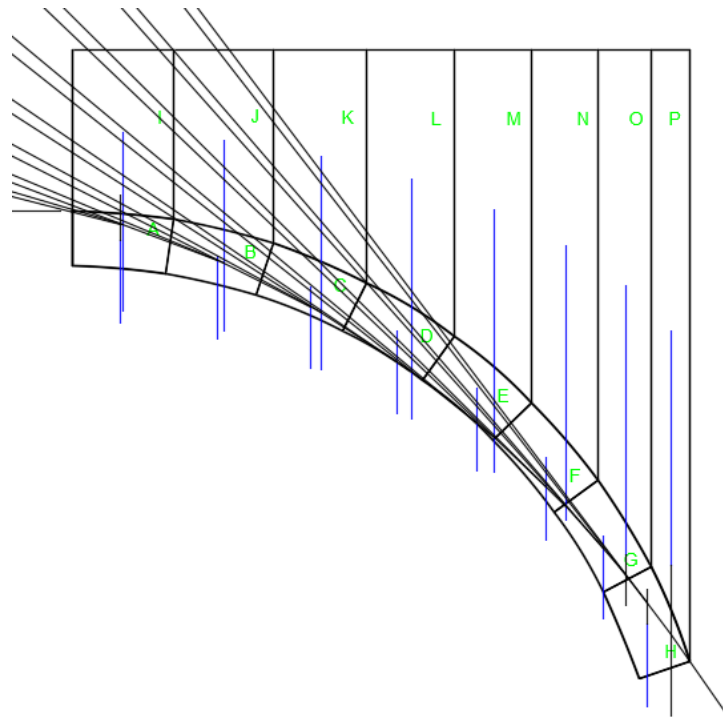


Figure 10 – Graphic statics thrust line

Zooming out, the critical value of the live load can be determined as the vertical component of the thrust line at the arch crown, illustrated below:

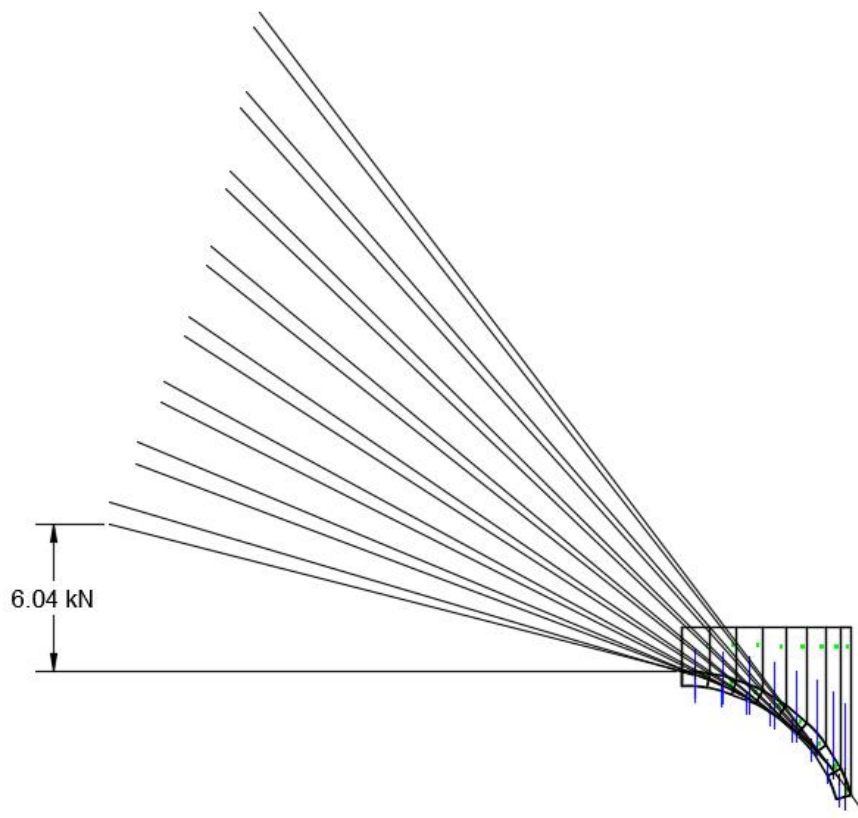


Figure 11 – Graphic statics load capacity

Converting this value to the critical force require multiplying by 2 (to account for the left side of the arch), and the scale factor of 73. This results in a critical load of 881.8 kN, corresponding to a load factor of 3.97.

## 4.2 Kinematic Analysis

The kinematic analysis was done using the same hinge locations as were used for the graphic statics analysis. The earth infill was divided into two blocks, and was assumed to rotate about the same point as the arch segment below. A graphic visualization of the analysis is shown in Figure 12, with the blue lines representing block weights, and the purple lines defining the centers of rotation. Table 5 lists the value of each load, its horizontal distance from its center of rotation, and the  $K$  factor which relates all rotation to a single point. As before, the analysis was done for a width of 1 m, and so the final result is multiplied by the width of the bridge.

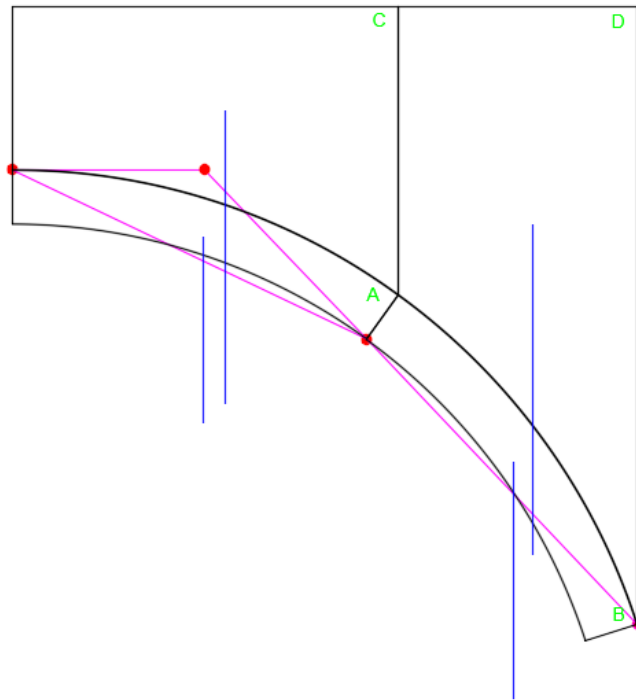


Figure 12 – Kinematic analysis divisions and loads

Table 5: Kinematic analysis summary

Member	Load	V	x	K
Block 1	A	73.84	0.008	-1.674
	C	184.62	0.226	-1.674
	Load	?	-2.140	-1.674
Block 2	B	73.84	-1.375	1.000
	D	233.84	-1.164	1.000

The unknown live load can be calculated by setting the work developed by external forces to zero, and then solving for the unknown load. This is shown in the following equation:

$$V_L = - \frac{V_A x_A K_A + V_B x_B K_B + V_C x_C K_C + V_D x_D K_D}{x_L K_L} \quad (4.1)$$

The result must then be multiplied by 2 (to account for the left side of the arch), and 3.65 m, the width of the bridge. This results in a critical load of 906.1 kN, corresponding to a load factor of 4.07.

### **4.3 Comparison**

There is a 2.5% difference between the critical loads calculated using the two methods. This is an acceptable level of convergence for limit analysis. The average of the two values, 4.02, is taken as the critical load. If the first iteration results in a large difference between the two methods, the assumed hinge locations can be adjusted until acceptable convergence is reached.

## 5 RIGID BLOCK ANALYSIS

The analysis program RING, which is based on the rigid block formulation, was used to model the masonry arch bridge with varying treatments of the infill. Analyses were also run with concentrated point loads, to compare with the limit analysis hand calculations reported above.

The effects of the infill on a masonry arch bridge can be divided into three categories, here denoted as I, II, and III:

- Effect I: Vertical weight of the infill
- Effect II: Distribution of load through the infill
- Effect III: Horizontal passive soil pressure activation

Analyses were run including effects I; I and II; I and III; and I, II, and III. This allows the relative significance of each effect to be determined. The final analysis, including all of the infill effects, corresponds most closely to reality and is taken as the predicted load capacity of the bridge for rigid block analysis.

Using only effect I, an additional analysis was run using a single equivalent point load (222.4 kN). Results are reported for the load applied both at midspan and off-center (the critical load). These results can be compared with the hand calculations above, but also show the difference between applying the load to single vs. tandem axles.

### 5.1 Modelling Assumptions

The RING bridge model is shown in Figure 13 below. Each arch was split into 55 stone voussoirs, based on the actual number of voussoirs visible in pictures of the bridge. The truck tandem axle was moved across the bridge in 10 cm increments. No partial factors were applied to either the loading or the materials. RING models the supports and embankments as rigid. The embankment length is automatically generated, and it sets the horizontal restraints sufficiently far from the arch that the rigid embankment does not artificially increase the arch stiffness.

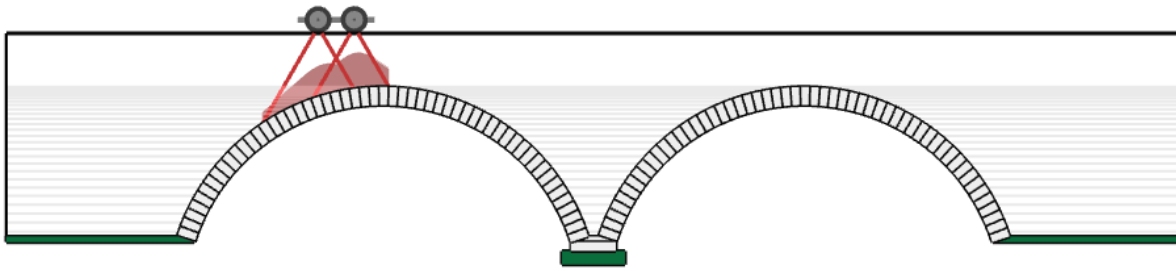


Figure 13 – RING model

The friction coefficient between blocks was taken as 0.6. The infill was modelled using the cohesion, angle of friction, and density parameters described in the Materials section above. Lacking more specific data, the default load dispersion, soil-arch interface, and passive zone parameters were used. These are shown in Figure 14. The factors  $m_p$  and  $m_{pc}$  are factors specific to RING, and they reduce the passive resistance associated with strength and cohesion respectively. The factor  $m_p$  is set to 0.33 to account for the curved surface of the arch and the likelihood that the full resistance is not activated at small displacements. Very little information is available on the effect of cohesion in masonry arch infill (RING, 2016), so its effect is limited to 5%.

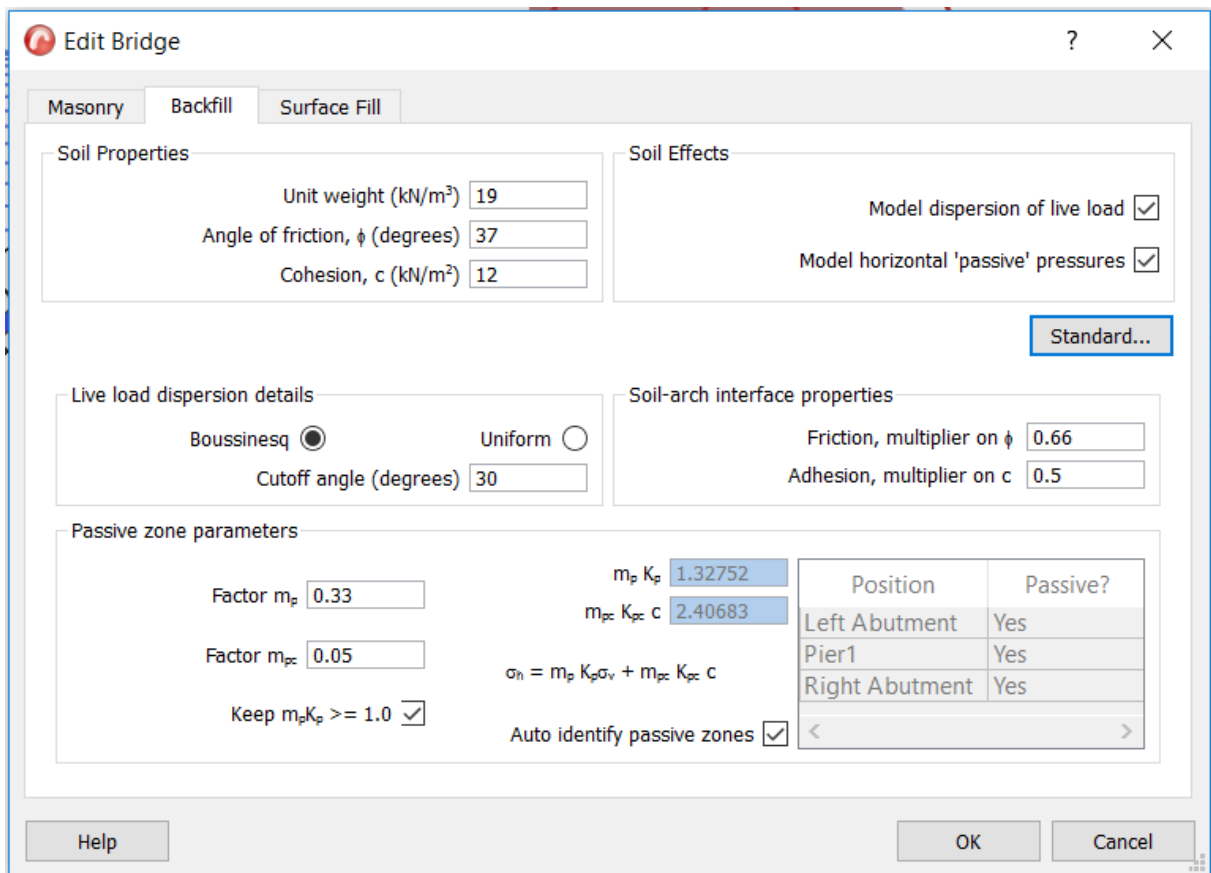
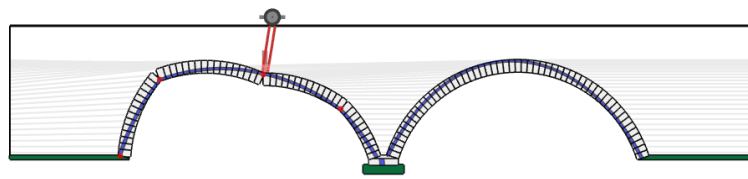


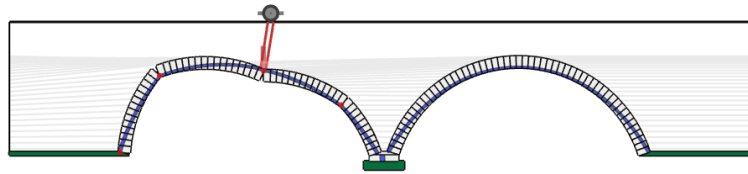
Figure 14 –RING soil properties

## 5.2 Results

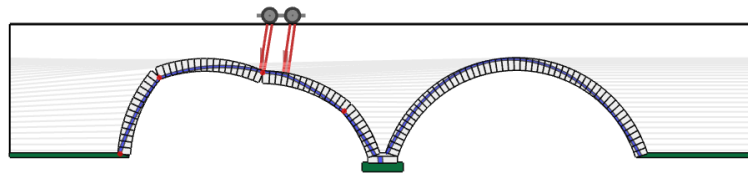
The results of the analyses are shown in Figure 15 below. The horizontal dark blue lines represent the activated passive pressure of the infill. The faded blue lines represent unactivated infill (RING ignores the relatively small “active” pressure resulting from arch movement away from the fill). For each test, RING reports an adequacy factor for each loading location along the length of the bridge. In the current case in which all partial factors are set to 1, the adequacy factor corresponds to a load multiplier. The resulting load factors are listed in Table 6.



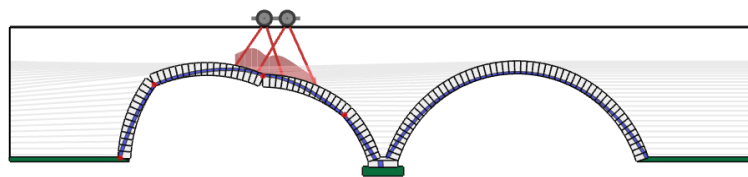
(a) Centered point load, infill effect I



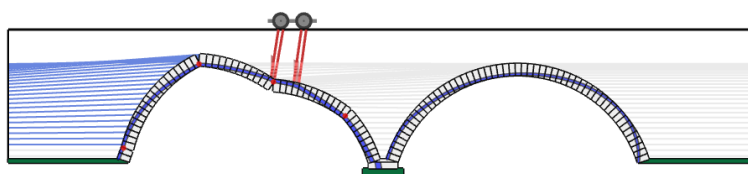
(b) Off-center point load, infill effect I



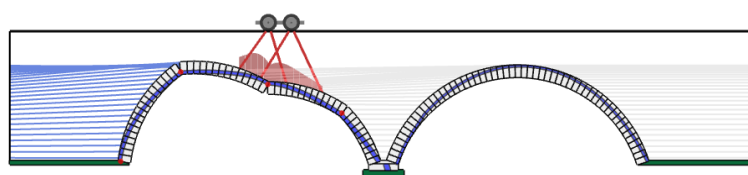
(c) Off-center tandem load, infill effect I



(d) Off-center tandem load, infill effects I and II



(e) Off-center tandem load, infill effects I and III



(f) Off-center tandem load, infill effects I, II, and III

Figure 15 –RING arch failure mechanisms



Table 6: RING load factor results

Analysis	Load	Infill	Load Factor
(a)	Point load, centered	I	3.14
(b)	Point load, off-center	I	2.78
(c)	Truck tandem, off-center	I	3.26
(d)		I, II	3.65
(e)		I, III	9.85
(f)		I, II, III	11.5

The results demonstrate the importance of the infill treatment on the load capacity of a masonry arch bridge. The effect of the horizontal passive pressure is especially significant, as it alone increases the estimated load capacity by a factor of three. The effect of load dispersion is less important, but it does provide a modest increase in load capacity. Comparing results (b) and (c) shows that a 17% increase in load capacity is observed when the load is applied to a tandem axle rather than a single axle.

The hand calculations gave a load factor of 4.02, while RING gives a factor of 3.14. The difference can be ascribed to RING's ability to limit the compressive strength. If the RING model is given infinite compressive strength, the resulting load factor is 4.32.

This page intentionally left blank.

## 6 FEM MODELLING ASSUMPTIONS

### 6.1 FEM Analysis with Smeared Crack Model

The finite element analysis program ATENA was used to run the FEM analysis with the smeared crack model. This program was used because it has been developed specifically for modelling the crack propagation and nonlinear effects of concrete, and thus the built-in material models can capture quasi-brittle behavior effectively. The use of these models is not technically correct for masonry, due to masonry's inherent anisotropy. However, it is a commonly used simplification, since the quasi-brittle models developed for concrete are well-tested and widely available. Roca *et al.* (2010) provide a review of analysis procedures for historic structures, including several FEM analyses of masonry using isotropic models. Anisotropic models exist (Lourenço, 1996), but in most cases have not yet been implemented in software packages. For these reasons, the isotropic model was used.

#### 6.1.1 Geometry and Mesh

The arch voussoirs were split into 12 elements, approximately square, through the thickness. This is necessary to allow for an accurate representation of crack propagation. Elsewhere in the model, a mesh size of 0.2 m was used, refined to 0.05 m near the supports and loading locations. Linear 4-noded elements were used throughout. The mesh is shown in Figure 16.

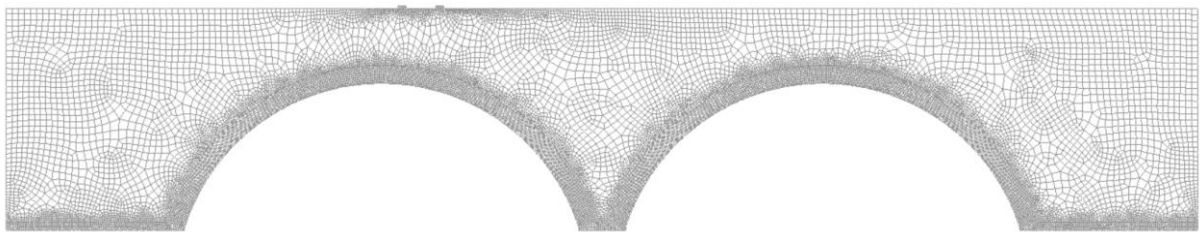


Figure 16 – ATENA mesh

#### 6.1.2 Materials

Using the macro-modelling simplification, the masonry was modelled as a homogenous isotropic continuum. The material model chosen to represent the masonry must be chosen with

care, since it must be able to adequately describe the quasi-brittle masonry characteristics. The tensile response is characterized by a small peak value followed by a steep softening curve. The compressive strength is much higher, but is nonlinear in the pre-peak region. Both responses are important, as they control crack propagation and the response of the compression ligament respectively. Using these characteristics, an approximate material model was chosen from the ATENA material library. The selected constitutive model is called *CC3DNonLinCementitious2*, and its main components are shown in Figure 17.

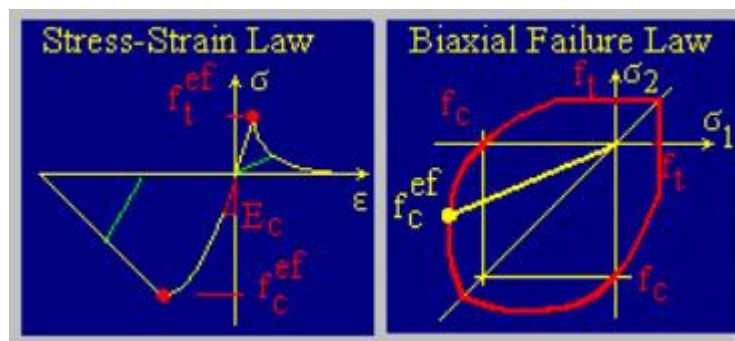


Figure 17 – ATENA masonry constitutive relationships

In compression, the model allows for pre-peak nonlinearity, but for simplicity, this portion of the curve was treated as fully elastic. The length of the yielding plateau is 0.000296 of strain, after which softening begins. The critical compressive displacement was 0.0005 m, meaning for the element size of 0.05 m, the strain at which softening has reduced the stress to zero is 0.01. The compressive portion of the uniaxial constitutive rule is shown in Figure 18. As stated earlier, an isotropic biaxial failure law was used for practical reasons.

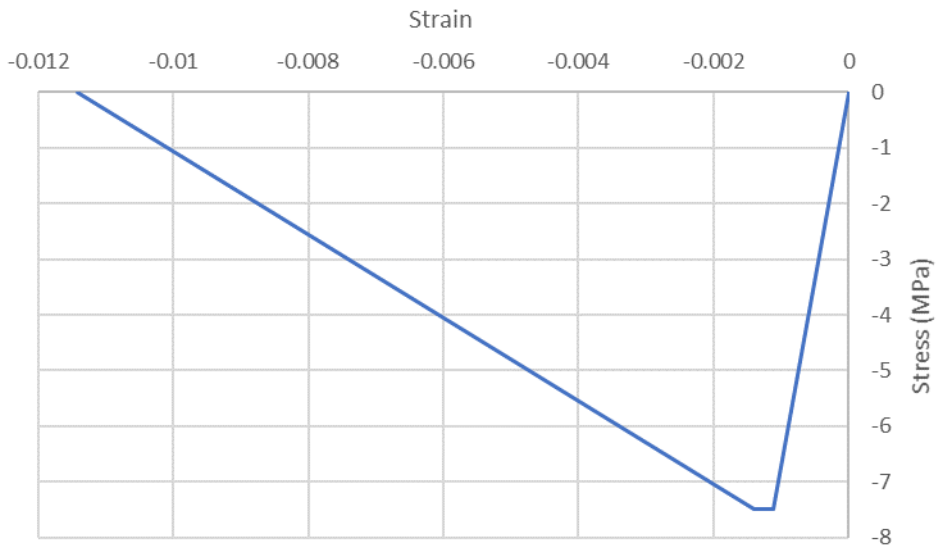


Figure 18 – ATENA compressive constitutive rule

In tension, a crack band model was used to represent the quasi-brittle behavior, and it is shown in Figure 19.

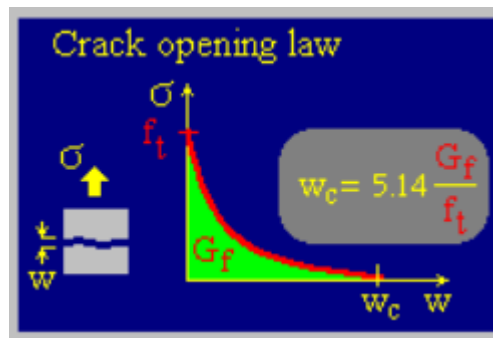


Figure 19 – ATENA crack opening law

The infill was modelled using the Drucker-Prager model for materials with internal friction. This model applies when yielding depends on the hydrostatic stress, and it is commonly used for soils and rocks. The strength properties of the soil depend only on the cohesion and the angle of friction. The yield surface is defined by the following equation:

$$\alpha I_1 + \sqrt{J_2} - k = 0 \quad (6.1)$$

where  $I_1$  is the first invariant of the stress,  $J_2$  is the second invariant of the deviatoric part of the stress, and  $\alpha$  and  $k$  are parameters controlling the shape and position of the yield surface. These parameters depend on the cohesion and angle of friction, and can be calculated by matching with the Mohr-Coulomb yield surface along the tensile meridian:

$$\alpha = \frac{2 \sin \phi}{\sqrt{3}(3 + \sin \phi)} \quad (6.2)$$

$$k = \frac{6c \cos \phi}{\sqrt{3}(3 + \sin \phi)} \quad (6.3)$$

Using the material properties specified above,  $\alpha = 0.192935$  and  $k = 0.0092172$  MPa. The ATENA model used is called *CC3DDruckerPragerPlasticity*, and exact information on it can be found in the ATENA Theory document. The failure function is shown in Figure 20. Perfect bond (i.e., no sliding) was assumed between the masonry extrados and the infill.

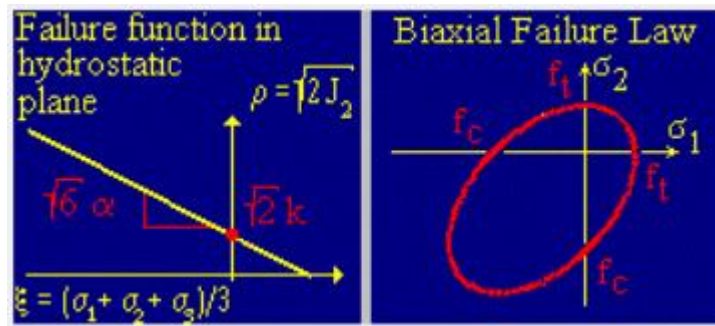


Figure 20 – ATENA Drucker Prager failure functions

### 6.1.3 Loading and Boundary Conditions

The truck tandem load was used, applied 1.28 m off-center. The loads were applied as point loads, and elastic steel plates measuring 25.4 cm x 8.5 cm were modeled to distribute the load over the width of the truck tire patch. Plates were introduced because they helped delay the development of convergence problems in the very low-stiffness infill. The dead load was

applied first, after which the live load was incrementally applied, while holding the dead load constant.

The arch was supported on trapezoidal elastic steel plates, measuring 35 cm in thickness, and tapering down to 10 cm at the arch springlines, which represents the nearly rigid foundation. These plates were inserted to provide a continuous support beneath both the masonry and infill, giving better stability to the model. Furthermore, the supports allowed for the vertical reaction forces to be measured directly, without needing to implement local axes.

Vertical boundary condition restraints were added beneath all of the steel support plates. This is a simplification, as all foundations have some finite stiffness. However, subsurface exploration borings performed during the 1986 Biggs and Rogers intervention confirmed that the foundations are bearing on shale. This means the simplification should not change the results significantly. Horizontal boundary conditions were added to the vertical edges of the infill and steel plates. Nodal

Additional nodal restraints preventing movement in the horizontal direction were added to the nodes at the base of the arch extrados on the embankment sides (these nodal boundary conditions cannot be seen in the model below). These restraints were added during one of the early troubleshooting operations, since these nodes are shared by all three materials (masonry, infill, and steel), and it was thought that stability issues might arise. Since the stiffness of the steel plate is very high regardless, the effect of these nodal restraints is insignificant.

The bridge model showing the masonry (yellow), infill (blue), and steel plates (green) is shown in Figure 21 below. The loading and boundary conditions are also shown.

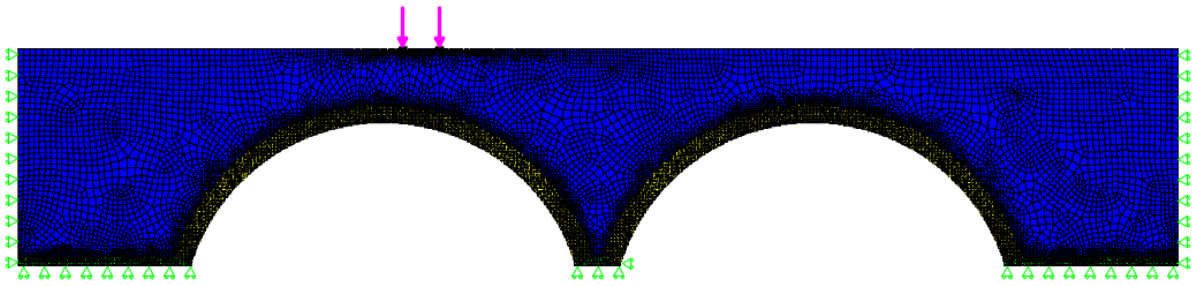


Figure 21 – ATENA materials, mesh, loading, and boundary conditions

#### 6.1.4 Method and Parameters of Nonlinear Solution

The Newton-Raphson method with load control was used to run the analysis. The arc-length method was attempted, but the Newton-Raphson method appeared to be more stable. All of the analyses failed to converge long before reaching a softening response, and so Newton-Raphson was deemed appropriate. Default solution parameters were used, except that the iteration limit was increased to 100. These parameters are shown in Figure 22.

Method	Newton-Raphson
Displacement Error	0.01
Residual Error	0.01
Absolute Residual Error	0.01
Energy Error	0.0001
Negligible Size Relative	0.00001
<input type="checkbox"/> Activate Negligible Size Absolute	
Iteration Limit	100
Optimize Band Width	Sloan
Stiffness Type	Tangent Predictor
Assemble Stiffness Matrix	Each Iteration
Solver	PARDISO
Solver Iter limit	10000
Extend Accuracy Factor	2.0
Pardiso Required accuracy	0.00000001
<input checked="" type="checkbox"/> Line-Search Method	
Line Search With Iterations	Line Search With Iterations
Unbalanced Energy Limit	0.8
Line Search Iteration Limit	3

Figure 22 – ATENA solution parameters



First, the dead load was applied in 10 equal steps. Then, for the live load, the load step was varied as follows: 8 steps using a step size of 0.25 (load factor 2), 50 steps using a step size of 0.2 (load factor 12), and all subsequent steps using a step size of 0.1. The loading was scaled such that one load step represented the load of a single truck.

## **6.2 FEM Analysis with Discrete Crack Model**

In many cases, FEM analysis programs do not have robust built-in quasi-brittle material models. This is true for concrete, but is even more so for masonry, which in reality has anisotropic, non-homogenous material properties. In these cases, the discrete crack model may be used instead. For masonry arch bridges, the hinge locations can be estimated a priori, and thus cracks can be represented by cohesive interfaces inserted along the edges of solid elements. The interfaces are then assigned material properties corresponding to the tensile strength and fracture energy parameters. The compressive material properties are less important, and can be represented with varying degrees of accuracy using elastic or elasto-plastic constitutive models. The finite element analysis program ADINA was used to run the FEM analysis with the discrete crack model. ADINA is a more general FEM program than ATENA, and it has the ability to model interfaces with specified cohesive properties.

Two loading conditions were studied using this model. The first loading condition was the same as that applied in ATENA and RING. The results of the ATENA and first ADINA model suggested that failure was occurring in the infill before the arch failure could be reached. For this reason, a second loading condition was developed in which a load described by a Boussinesq distribution was applied directly to the arch extrados. The details of both models are discussed below.

### **6.2.1 Geometry and Mesh**

ADINA requires that surfaces to be meshed must have no more than four sides. Thus the model was split into the four-sided surfaces shown in Figure 23 below. Each surface was then meshed as follows. The arch voussoirs were split into 6 longitudinal rows, and the radial lines were

defined in such a way as to yield approximately square elements. The infill was meshed automatically using a mesh size of 0.254 m, shrinking to 0.127 m in the more critical regions beneath the load. Linear 4-noded elements were used throughout. The mesh is shown in Figure 24, with red, green, and purple corresponding to the infill, masonry, and supports respectively.

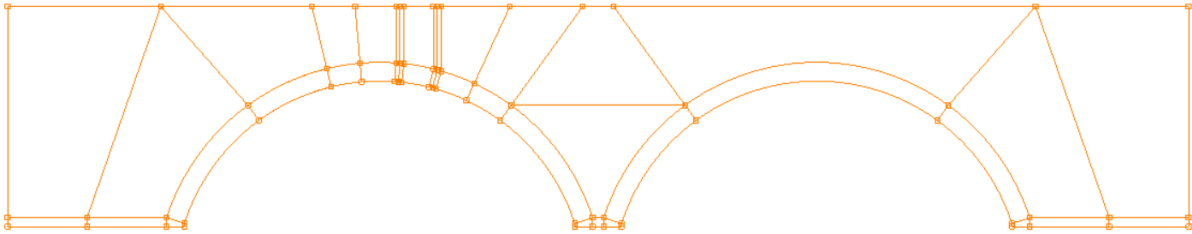


Figure 23 – ADINA surface distribution

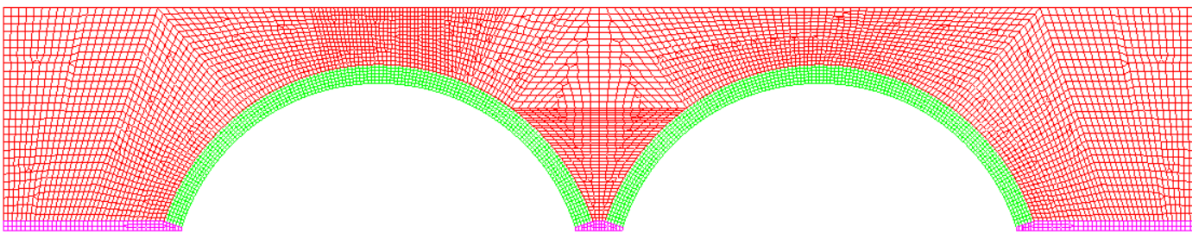


Figure 24 – ADINA mesh

### 6.2.2 Materials

The masonry was initially modelled as perfectly elastic, since failure in tension was expected to be critical. It was found, however, that this assumption greatly overestimated the stiffness and strength of the compressive ligaments above the crack opening locations. Thus an elastic-perfectly-plastic model was used instead. No hardening or softening was used in the model, and there was no ultimate cutoff strain. The initial modulus of elasticity, 6.75 GPa, was used up until the yield strength of 7.5 MPa. In biaxial compression, the von Mises yield condition was used. This is a large simplification, but it can be justified by the fact that at high loading levels, the stress in the compressive ligaments is nearly uniaxial.

The infill was modelled using the built-in Drucker-Prager material model. All parameters were the same as those defined in the Material Properties and ATENA sections above. No caps were applied to either the tension or compression response.

### 6.2.3 Loading and Boundary Conditions

The same boundary conditions used in the ATENA model were used here. Namely, vertical restraints beneath the steel support plates, and horizontal restraints on the vertical edges of the infill and steel support plates. The boundary conditions are shown in Figure 25.

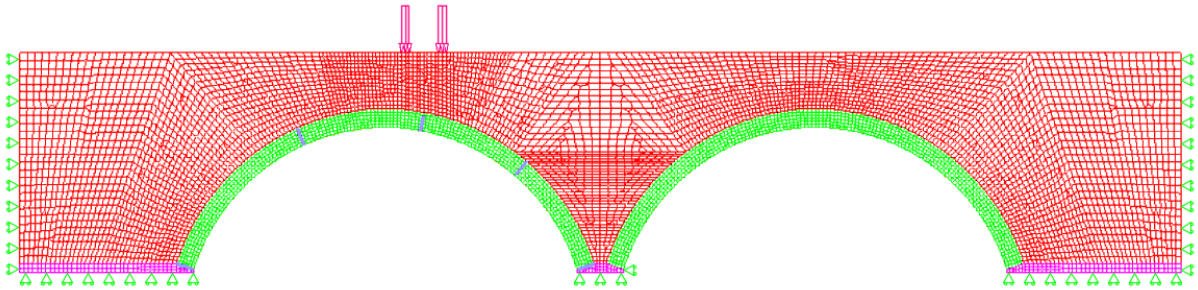


Figure 25 – ADINA hinge locations, TL loading, and boundary conditions

The first analysis was run using the same loading conditions used in the ATENA model, with the only difference being that the load was applied directly to the infill as distributed loads over the tire patch widths. This was done because ADINA's Drucker-Prager material model had convergence problems when steel plates were used. As before, the dead load was applied first and held constant, after which the live load was incrementally applied.

In order to investigate the load capacity of the arch without relying on the limited ability of the infill to transfer load, a second loading condition was developed using a Boussinesq load distribution applied directly to the arch extrados. This distribution model was selected since RING also uses a Boussinesq load distribution model. The RING user manual notes that the model is not entirely appropriate, since the soil does not remain elastic, and the space beneath the load is not semi-infinite; however, it still provides a useful means of generating a suitable

bell-shaped curve. The applicability of this model to masonry arch infill structures is further discussed in section 7.5 below.

This distribution was determined by calculating the Boussinesq stress at every point for each of the tire patches, and then summing the two effects. The following equation describes the Boussinesq distribution:

$$\sigma_z = \frac{q}{\pi} (\alpha + \sin(\alpha) \cos(\alpha + 2\beta)) \quad (6.4)$$

The variable definitions can be seen in Figure 26 below. The distributed load  $q$  was determined by dividing one truck axle by the tire patch width. The Boussinesq distribution was applied on a horizontal line 1.81 m below the surface, corresponding to the extrados of the arch crown. The distribution was cut off 3 m away from the load center on each side, in order to avoid the hinges propagating from the extrados. The vertical stress calculated along the horizontal line was then applied to the curved surface directly below.

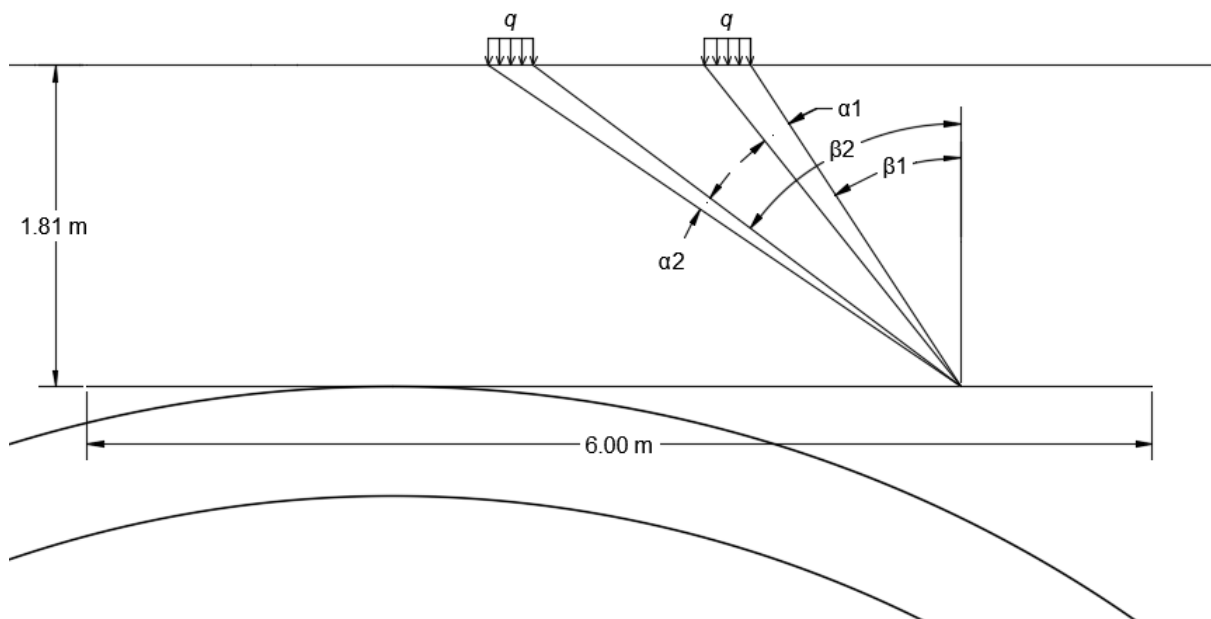


Figure 26 – Boussinesq loading calculations

The resulting Boussinesq load distribution applied to the ADINA model is shown in Figure 27.

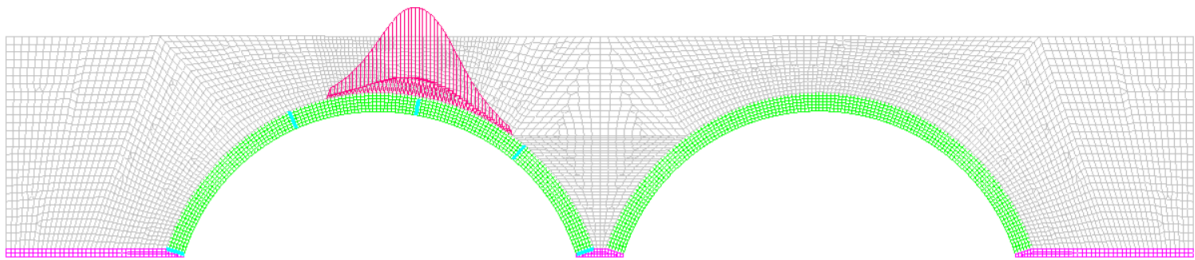


Figure 27 – ADINA Boussinesq loading

#### 6.2.4 Cohesive Interfaces

Cohesive interfaces can be defined along geometrical lines or mesh element edges. Where a cohesive interface is defined, the mesh nodes are duplicated and zero-thickness 4-noded elements are inserted, allowing opening and sliding between adjacent solid elements. The material properties governing tension, shear, and compression must then be defined. These properties are shown in Figure 28 with base units of kN and m. Mode I failure is tension, and the fracture “toughness” is the fracture energy. The normal cohesive strength is the tensile strength. The mode II parameters correspond to shear, and using a common simplification are here taken as three times the tension parameters. Sliding was not anticipated to be the critical failure mechanism. The penalty factor specifies the interface stiffness prior to failure and in compression. In this case, it was set to allow penetration of 0.01 mm at the compressive yield strength of 7.5 MPa.

The screenshot shows the ADINA software interface for defining cohesive interface properties. At the top, there are five buttons: 'Add...', 'Delete', 'Copy...', 'Save', and 'Discard'. Below these is a dropdown menu for 'Property Set #' with the value '1'. The 'Fracture Toughness' section contains two input fields: 'Mode I:' with the value '0.002175' and 'Mode II:' with the value '0.06525'. The 'Cohesive Strength of Interface in Direction' section contains two input fields: 'Normal:' with the value '150' and 'Shear:' with the value '450'. The 'Penalty' field has the value '750000000'. The 'Mixed-Mode Interaction' section contains a dropdown menu for 'Criterion' with the value 'Power Law' and an input field for 'Parameter:' with the value '1'. At the bottom right, there are two buttons: 'OK' and 'Cancel'.

Figure 28 – ADINA cohesive interface properties (base units kN and m)

The hinge locations must be specified manually, but an iterative process can be used to refine their locations. For this study, the locations calculated using RING were used as a first guess, and then moved to locations showing the highest concentrations of tensile stresses. Figure 29 shows one of the first iterations using the RING hinge locations, shown in red. The maximum principal stresses are shown in pink, and clearly do not correspond with the hinge locations. Thus the left and right hinge locations were moved closer to the center of the arch. Note that the Boussinesq load shown was one of the earlier iterations, and was later updated to be continuous over all of the line segments. It did not significantly alter the results however. The same hinge locations were used for both the Boussinesq and tandem load scenarios.

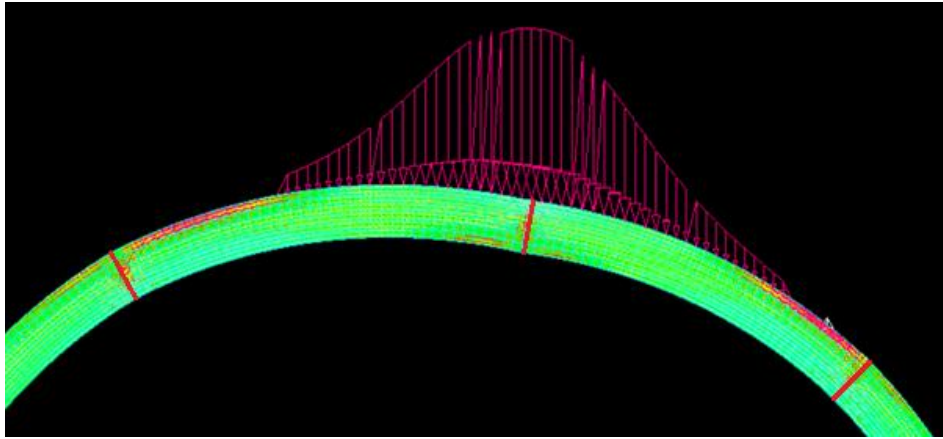


Figure 29 – ADINA hinge location iteration

The process is somewhat inexact, as the locations of maximum stress vary during the loading process, and also depend on the type of applied load. It is not expected that small differences in the hinge locations will have large effects on the final results, however. The final hinge locations selected are shown in Figure 25 above. The top cohesive interface was only applied to the lower five of the six elements, since the arch extrados load could not be applied at a duplicated node. As the top element must be in compression for the arch to be stable, this simplification is acceptable.

### 6.2.5 Method and Parameters of Nonlinear Solution

The Newton-Raphson method with load control was also used for the ADINA analysis. Default parameters were used, except that the maximum iteration limit was increased to 200. The parameters are listed in Figure 30.

Parameter	Value
Convergence	Energy
Energy Tolerance:	0
Contact Force Tolerance:	0.05
Minimum Reference Contact	0.01
<b>Line Search Settings</b>	
Convergence Tolerance:	0.5
Energy	0
Upper Bound:	0
Lower Bound:	0.001
<b>Force Tolerances</b>	
Force (Moment) Tolerance:	0.01
Reference Force:	0
Reference Moment:	0
<b>Displacement Tolerances</b>	
Translation (Rotation)	0.01
Reference	0
Reference Rotation:	0
Maximum Incremental Displacement in Any	0

Figure 30 – ADINA solution parameters

The dead load was first applied in ten equal steps. Then, the live loads were incrementally applied. For the model with load applied to the infill, the live load step size was 0.15. For the model with Boussinesq loading, the live load step size was 0.20 for the first 65 steps (up to load factor 13), and 0.40 thereafter. The load step was increased to bypass oscillating convergence issues that developed around load step 13. Smaller load steps were attempted, but only the larger steps were able to advance the model past these convergence issues.



## 7 FINITE ELEMENT ANALYSIS RESULTS

### 7.1 Global Response

The analysis of all three models ended by failure to reach convergence. The load-displacement curves for the three models are superimposed in Figure 31. The displacement is measured at the arch crown intrados, while the load factor is a direct multiple of the 222.4 kN truck load. Model nomenclature specifies analysis program and load type (TL = tandem load applied on top of infill, BSQ = Boussinesq load applied to arch extrados). The load factor applies only to the live load (full dead load applied at LF = 0). Up to a load factor of 5, the responses are very similar, but they begin to diverge at higher loads. The smeared crack (ATENA-TL) model shows the lowest stiffness, probably due to its ability to open many different cracks. At higher loads, material softening effects may also reduce the stiffness. The discrete crack model with Boussinesq loading (ADINA-BSQ) has the highest stiffness. This makes sense, since it has the lowest ability to redistribute load over the course of the analysis.

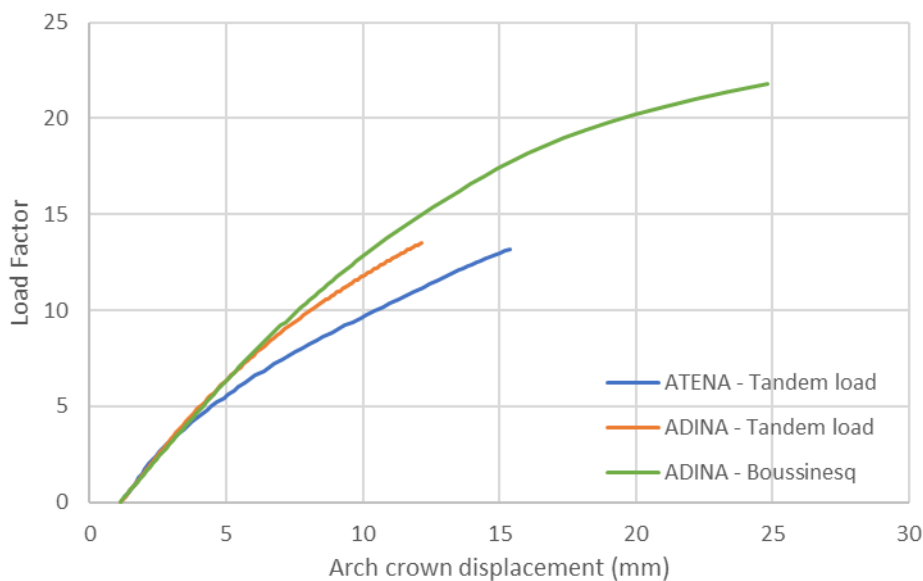


Figure 31 – FEM load-displacement plot

For the models with the load applied to the top of the infill, both in ATENA and ADINA, convergence issues occurred at very similar load factors of 13.2 and 13.5 respectively. The text

output of the ADINA model specifies that the analysis is stopped due to “No convergence in the Drucker-Prager material model.” This supports the hypothesis that failure occurs in the infill prior to failure of the arch.

The discrete crack model with load applied directly to the arch extrados reached a load factor of 21.8 before failing to converge. The analysis was solved using large displacements. At higher load levels, the solution process tended to oscillate, so the step size was increased from 0.2 to 0.4. As the Newton-Raphson method was being used, the ability to approach the peak load was limited, particularly with these large load steps. However, significant pre-peak nonlinearity can be observed, and it is likely that the arch in this model is close to failure. It is hypothesized that the infill failure observed in the previous models is merely the result of modelling assumptions, and has no real meaning. However, further study is needed before firm conclusions can be drawn. If it is determined that the infill failure can safely be ignored, a Boussinesq load distribution on the arch extrados is a conservative but realistic way to load the arch.

## **7.2 Crack Patterns and Deformation**

The deformation plots showing either crack opening for all models are given below. These plots show the models just prior to divergence, at the highest load levels recorded. Note that a deformation multiplier of 20 is used, since even at very high loads, the arch deformation is nearly imperceptible. The maximum recorded crack width for the three models are 4.64 mm, 5.35 mm, and 12.52 mm respectively.

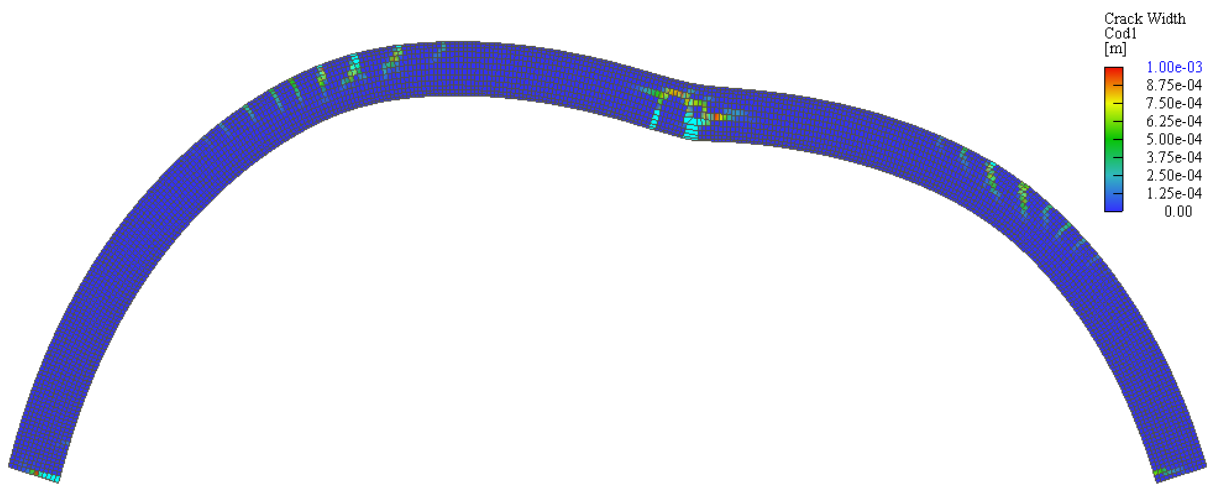


Figure 32 – ATENA-TL crack map with 20x deformation (LF = 13.2)

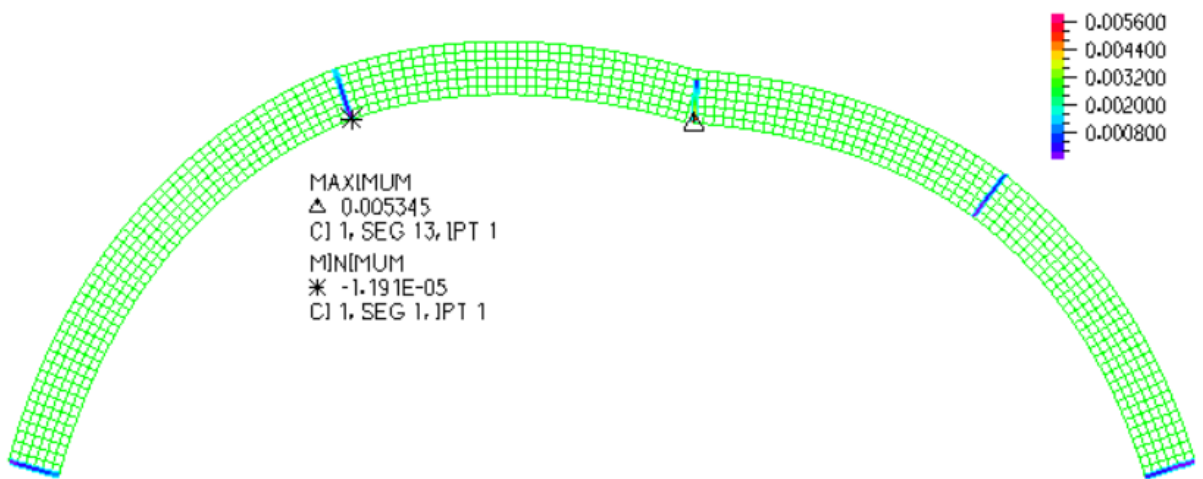


Figure 33 – ADINA-TL crack opening with 20x deformation (LF = 13.5)

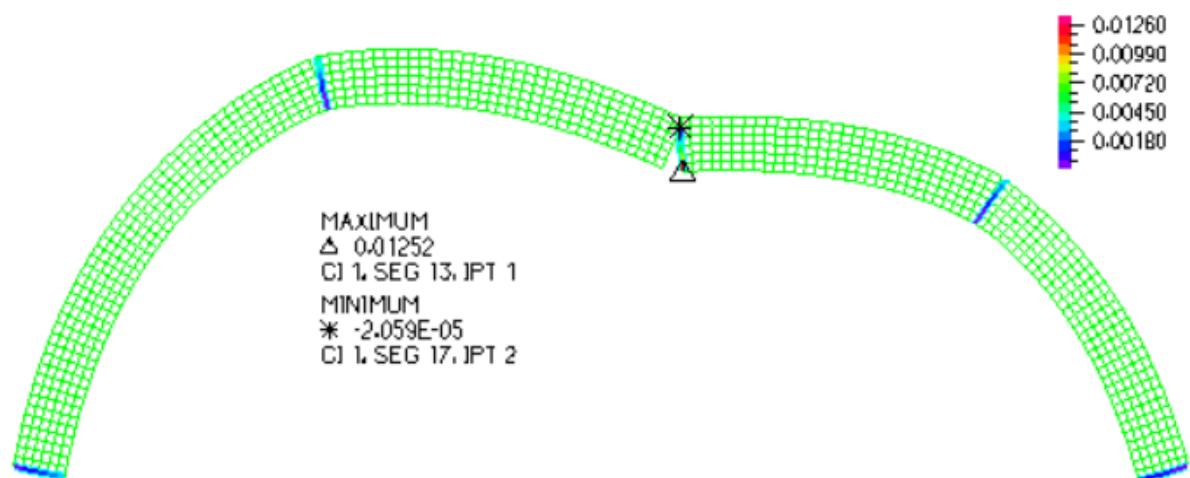


Figure 34 – ADINA-BSQ crack opening with 20x deformation (LF = 21.8)

### 7.3 Critical State Analysis

For the purpose of better understanding intermediate loading states, four critical states of the structure were defined, and they are listed below. The load factors (LF) determined at these critical states are given in Table 7. These states are defined as follows:

- 67% Compression: This is the service level criterion used by Biggs and Rogers (1987), and it is included here for comparison. This limit is reached when the bottom third of the center hinge is in tension.
- Fourth hinge initiation: This limit is reached when crack opening has initiated at all four hinges. This is an alternative service-level criterion, and it is still conservative, as the hinge initiation occurs long before the full hinge development.
- Compression yield strength reached: This limit is reached when the compression strength at the extreme compressive fibers of one of the hinge locations is reached. For the bridge in question, this occurred prior to arch failure in all models. It is expected that this would hold true in general, but more study may be needed to prove this, especially for materials with high compressive strengths. After this point, softening can be expected to occur, which may or may not be adequately accounted for in the FEM model used. The ATENA model incorporated softening, but the ADINA model did not.
- Maximum load factor attained: This limit is self-explanatory, but it should be noted that it does not necessarily correspond to the failure of the arch itself, as failure of the infill can occur first. Furthermore, simplifications in the interfaces and material models become less reliable at high levels of loading. Thus these values should be treated with care.

Table 7: FEM load factors at critical steps

Model	Load Factor			
	67% Compression	Fourth hinge initiation	Compression yield strength reached	Max. load factor attained
ATENA-TL	3.2	5.8	9.4	13.2
ADINA-TL	3.6	7.6	8.8	13.5
ADINA-BSQ	4.0	9.6	10.8	21.8

In ADINA, the first two criteria were determined using the effective stress and stress vector plots. In ATENA, these options are not available, so the principal stress and crack opening plots were used instead. Cracks smaller than 0.01 mm were disregarded. Plots of the critical section of each model at 67% compression are shown in Figures 35 to 37. Plots of the fourth hinge at first opening are shown in Figures 38 to 40. The plots of cohesive normal stress show that even though a small tensile strength is used, the interface quickly becomes tension-free.

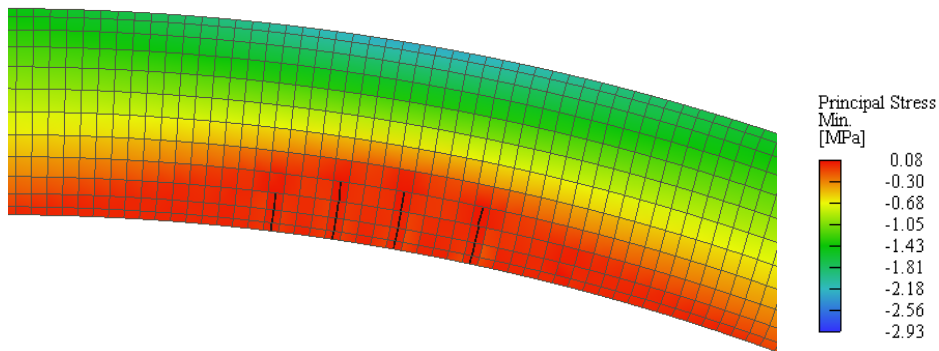


Figure 35 – ATENA-TL at 67% compression (LF 3.2)

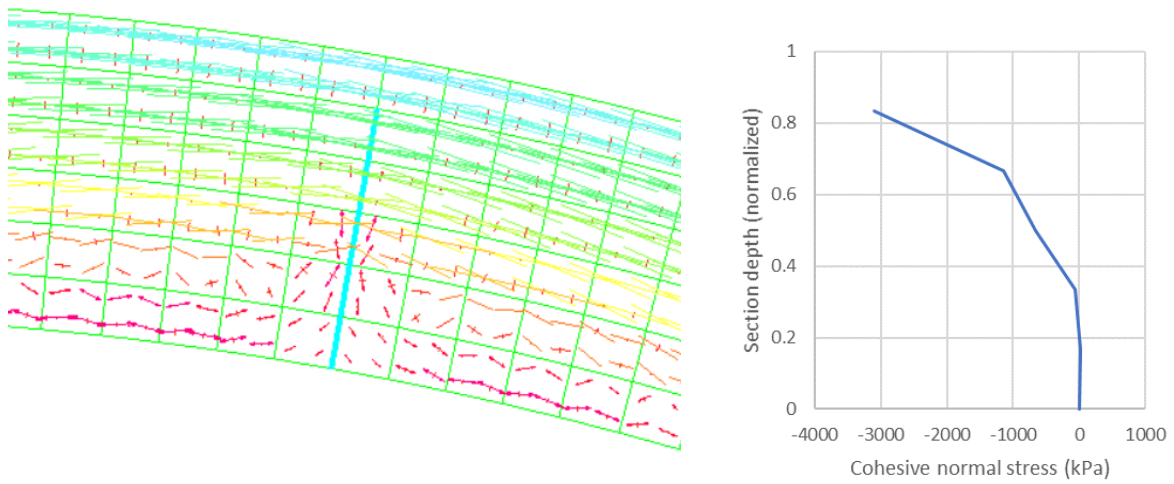


Figure 36 – ADINA-TL at 67% compression (LF = 3.6)

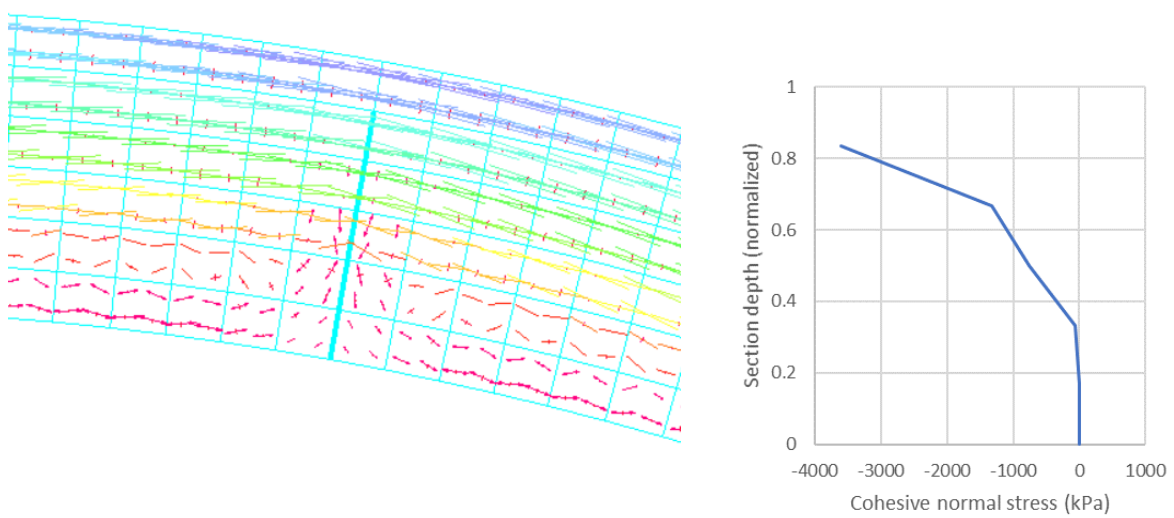


Figure 37 – ADINA-BSQ at 67% compression (LF = 4.0)

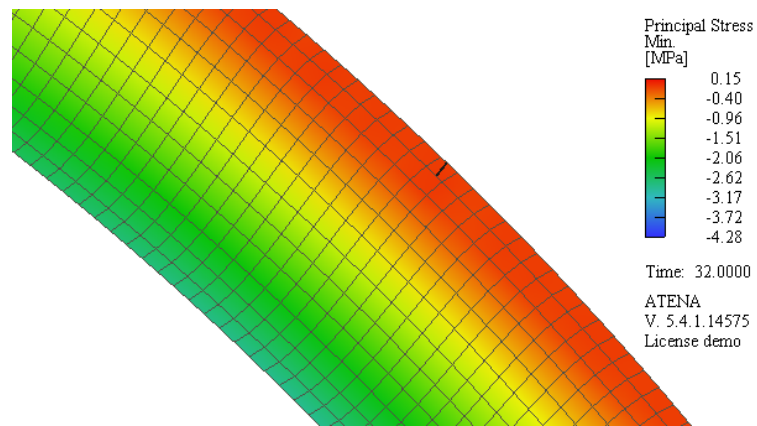


Figure 38 – ATENA-TL fourth hinge initiation (LF = 5.8)

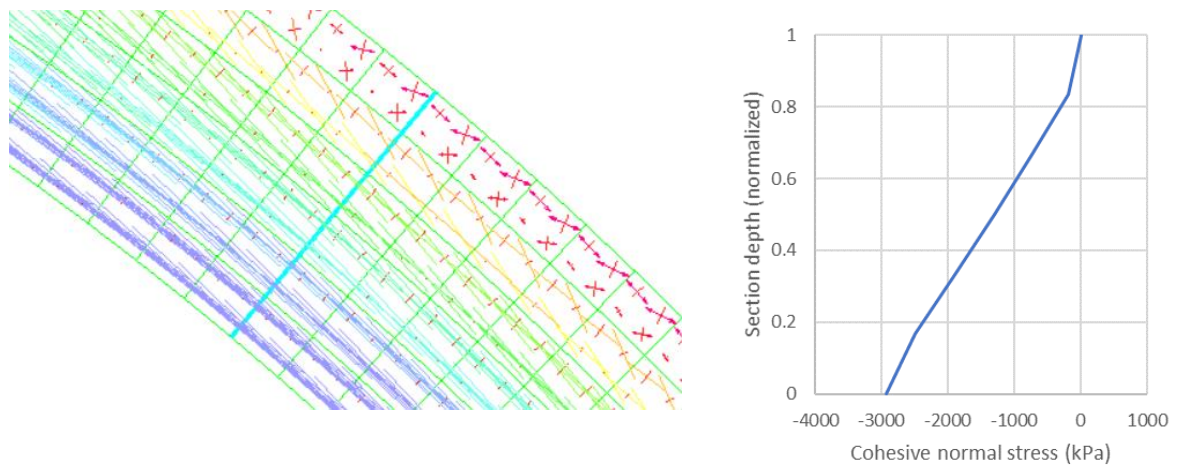


Figure 39 – ADINA-TL at fourth hinge initiation (LF = 7.6)

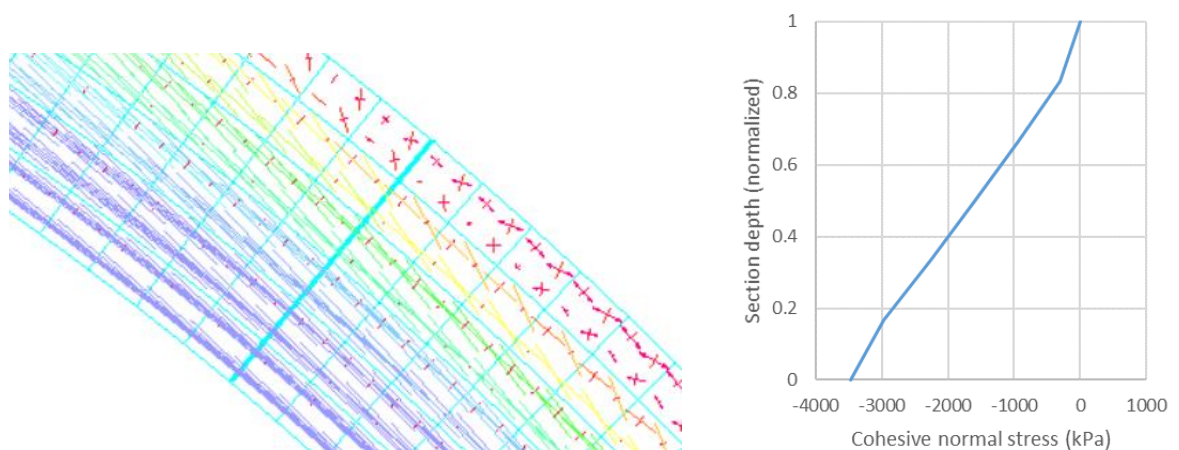


Figure 40 – ADINA-BSQ at fourth hinge initiation (LF = 9.6)

The compression yield strength was identified by the first appearance of plastic strain. This was sufficient for the material models used, since the masonry was assumed to be elastic up until yield. Plots of the models at the initiation of yielding in compression are shown in Figures 41 to 43. The blue box in the ATENA screenshot highlights the integration points at which plastic strain has begun to occur (shown in orange).



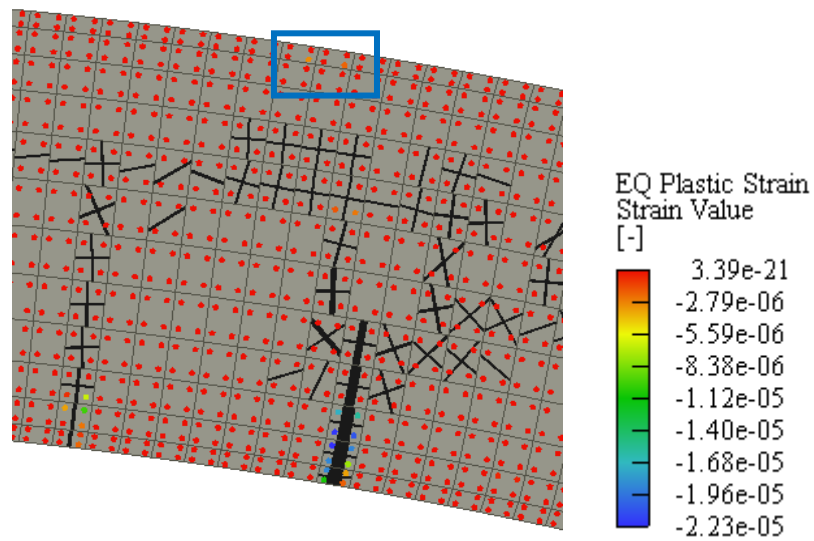


Figure 41 – ATENA at first compressive plastic strain (LF = 9.4)

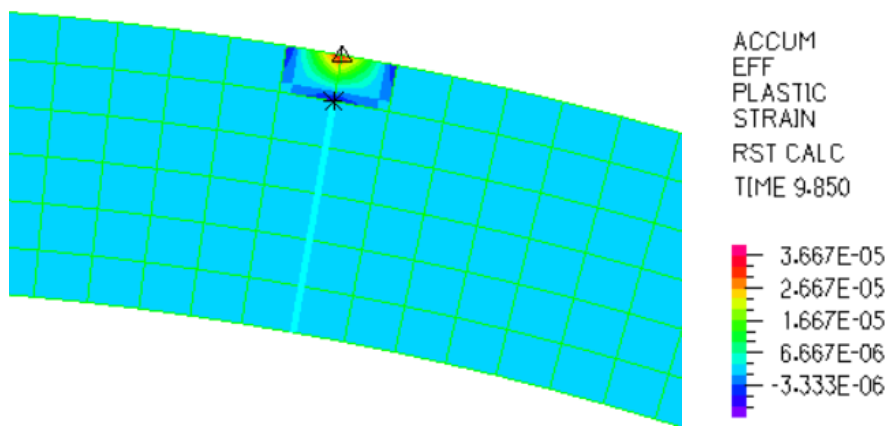


Figure 42 – ADINA-TL at first compressive plastic strain (LF = 8.8)

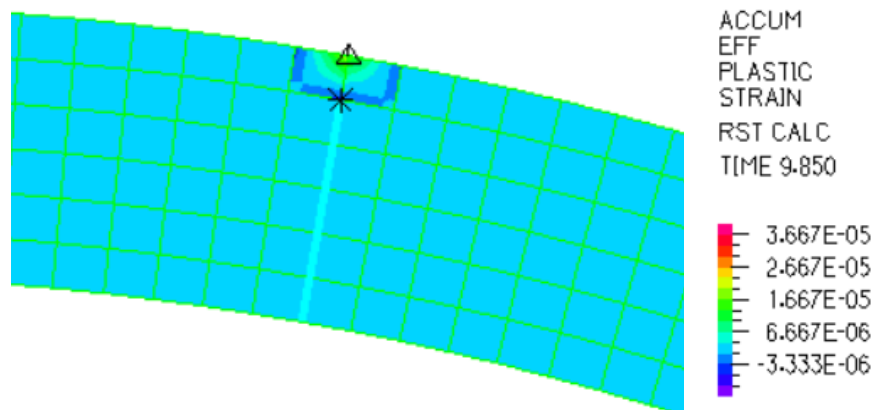


Figure 43 – ADINA-BSQ at first compressive plastic strain (LF = 10.8)

One of the key findings of this analysis is the wide range of loading values over which failure occurs. The ratios between the first (67% compression) and third (compression strength reached) criteria are 2.94, 2.44, and 2.70 for the three models respectively. This means that the lower service-level criteria may be used with a high level of confidence.

Up until the point at which compressive nonlinearity begins, the models give consistent results. The ADINA-BSQ model, being the stiffest, gives load capacities slightly higher than the other two models, but they are within the same range. Beyond this point, the assumptions and simplifications used in the models have larger effects, and the results begin to diverge. Softening in the masonry occurs in the ATENA model, giving a less stiff result. For both models using load dispersion through the infill, failure occurs in the infill before the load capacity of the arch is reached. If the infill is prevented from failing, much higher loads can be reached. However, this may be unconservative. These results indicate that more detailed analyses may be necessary to adequately capture the nonlinear behaviour of masonry arches.

#### **7.4 Comparison with Biggs and Rogers 1987 Analysis**

Biggs and Rogers (1987) calculated the compressive stress and percent contact area resulting from a single truck load. The details of this analysis are given in section 3.2 above. Since this report used allowable stress design, the load factor causing collapse was not calculated, making comparison with the present report difficult. Approximate comparisons, however, can demonstrate that the results of the 1987 report were conservative in comparison to the modern methods presented here.

If it is assumed that, since the analysis is linear, doubling the load will double the stress at the critical section, the load factor causing failure can be extrapolated approximately from the reported data. The compressive limit state is 2.76 MPa, and the dead load plus a single truck results in a stress of 2.25 MPa. The dead load accounts for 1.84 MPa, meaning the live load causes 0.41 MPa of compressive stress. This results in a load factor of 2.24, which is very conservative compared to the FEM results in the present study. Compressive yielding is reached at load factors ranging from 8.8 to 10.8 in the FEM models created for this study. Most of this difference can be ascribed to the fact that the full material strength is used in the FEM models,

while Biggs and Rogers used a reduced compressive strength. The ratio between the compressive strengths used is 2.72, within the range of typical ASD reduction factors.

For the purpose of rating the bridge, the fourth hinge initiation criterion was deemed acceptably conservative. Averaging the two cases with load applied on top of the infill gives a load factor of 6.7. This applies for static loading only. Reducing by the AASHTO dynamic loading factor of 1.33 gives a load rating of 5.0. The bridge is thus sufficient for the applied loads, and has significant overcapacity.

### 7.5 Boussinesq Load Verification

In order to determine the accuracy of the Boussinesq load in representing the actual distribution through the infill, the vertical stress along the arch extrados was recorded using the ADINA-TL model (i.e., with load applied to the top of the infill). The stress resulting from the full application of the infill dead load was subtracted from the measured stress at each load step, giving the stress resulting from the live load alone. The resulting stress distributions at varying load factors are shown in Figure 44.

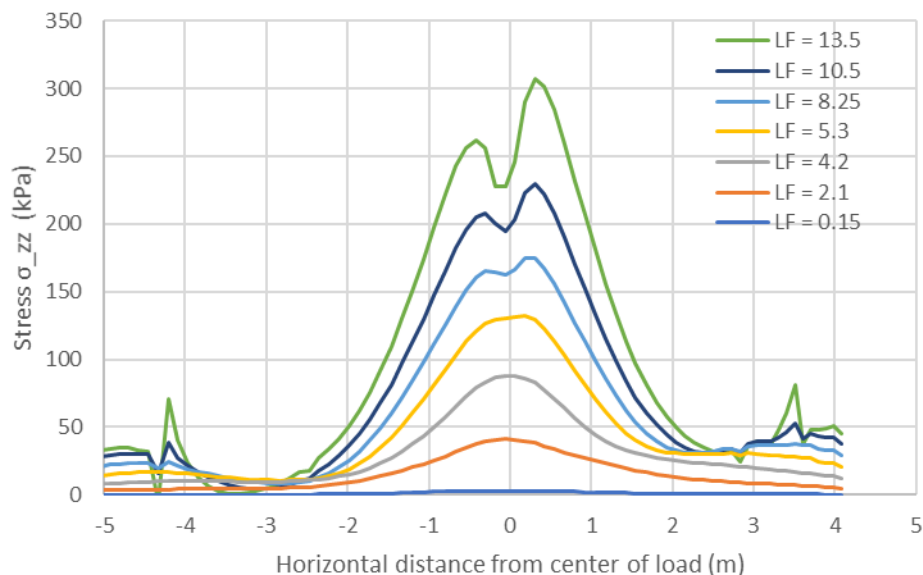


Figure 44 – ADINA-TL measured vertical stress along arch extrados

It can be seen that, as expected, the distribution is roughly bell-shaped, though even from the start the stiffer right-hand side carries more load. At higher load levels, each axle's bell shaped distribution falls off rapidly towards the center, as the arch is deflecting the most directly beneath the center of loading. This results in a curve with two peaks. The discontinuities on the left and right side correspond to the hinge locations, and have high values because the arch movement into the infill is highest at these locations.

For further comparison, the calculated Boussinesq distribution was plotted for load factors of 2.1, 8.25, and 13.5. Comparison of these values with the measured ADINA values are shown in Figures 45 to 47. Note that the Boussinesq load is cut off 3 m away from the center on both sides.

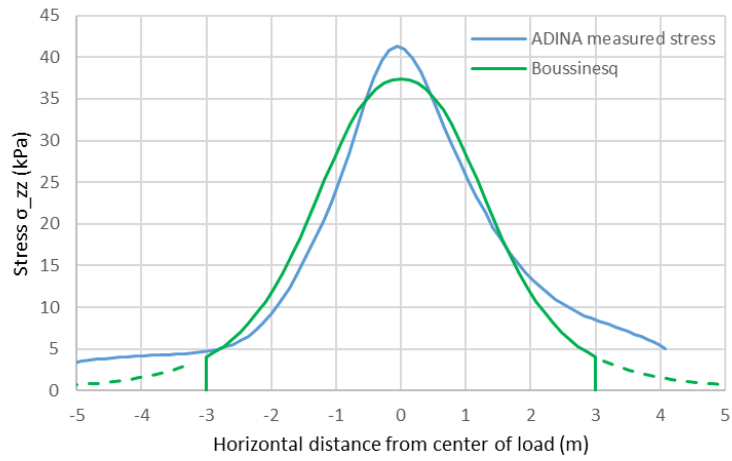


Figure 45 – Boussinesq vs ADINA loading at LF 2.1

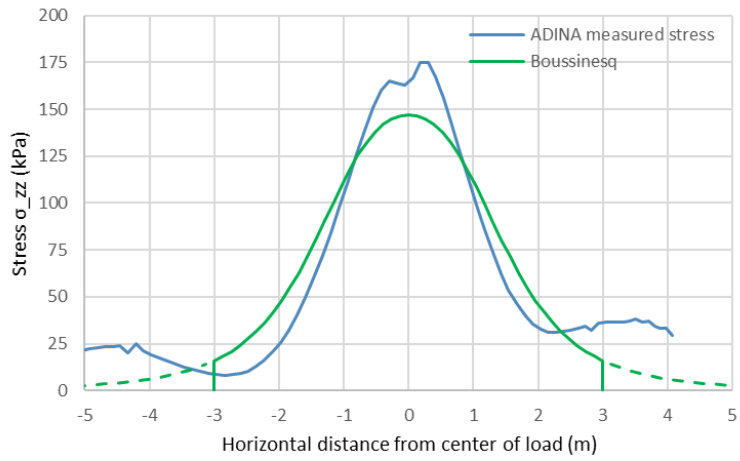


Figure 46 – Boussinesq vs ADINA loading at LF 8.25

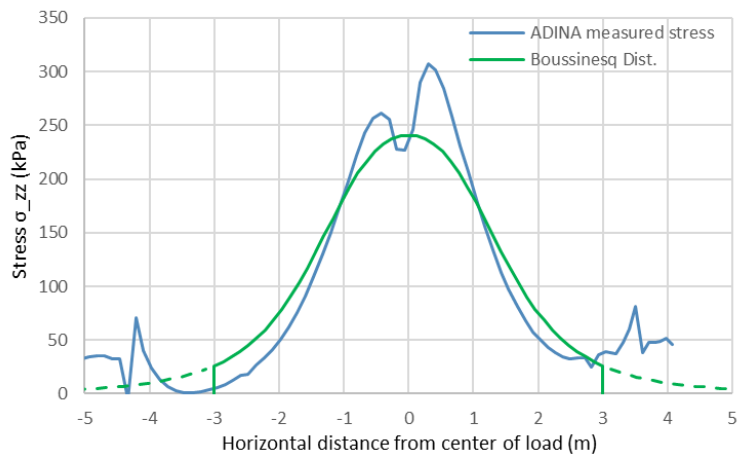


Figure 47 – Boussinesq vs ADINA loading at LF 13.5

The results show that the measured distribution is more concentrated than the Boussinesq distribution, particularly at higher loads. On the other hand, the measured distribution has higher values than the Boussinesq distribution at the tail ends, especially if the Boussinesq load is cut off. This may be due to some limited arching capacity within the infill redistributing the infill self-weight towards the sides of the arch. This phenomenon would have the effect of stabilizing the arch, meaning the Boussinesq distribution is likely conservative.

Despite these differences, the Boussinesq distribution appears to adequately describe the effects of load dispersion in the infill, particularly at lower load levels. Thus the load dispersion effects are not likely to be the main cause of discrepancies between the two loading models used in the discrete crack model. This result does, however, provide justification for RING's use of a Boussinesq distribution.

## 8 DISCUSSION

The key modelling assumptions and calculated load factors are summarized in Table 8 below. The load factor specifies how many multiples of the AASHTO truck load used in this study can be applied to the bridge, assuming static loading. The weight of the truck is 222.4 kN, and it is split between two axles. For the limit analysis and rigid-block models, the LF is the calculated failure load divided by the weight of a single truck. For the FEM models, the bridge was first loaded with the self-weight of the bridge. The self-weight was then kept constant while the live load was incrementally increased until the analysis failed to converge.

The RING results show that including the infill passive soil pressure has a large effect on the calculated load capacity. Thus any calculation methods that do not include this effect, such as the “by-hand” calculations, are likely to be very conservative. Furthermore, the more detailed and automated RING analyses allow for greater analytical confidence.

The second key finding is that the rigid-block analysis can provide estimated load capacities nearly equaling those calculated using the FEM analyses. This is significant, because the time and computational effort required for a RING analysis is much smaller than that required for a full FEM analysis.

Table 8: Load factor summary for all models

Program	Load	Hinges	Infill	Tensile strength	Load Factor
Limit analysis	Point load, centered	S	I	0	4.02
Rigid block (RING)	Point load, centered	C	I	0	3.14
	Point load, off-center	C	I	0	2.78
	Truck tandem, off-center	C	I	0	3.26
		C	I, II	0	3.65
		C	I, III	0	9.85
		C	I, II, III	0	11.5
FEM smeared crack (ATENA)	Truck tandem, off-center	C	I, II, III	$2\% f_m$	13.2
FEM discrete crack (ADINA)	Truck tandem, off-center	S	I, II, III	$2\% f_m$	13.5
	Truck tandem, off-center (Boussinesq)	S	I, II (B), III	$2\% f_m$	21.8

S = hinge location user-specified, C = hinge location calculated by program  
I = vertical weight, II = load dispersion, III = horizontal passive pressure  
B = dispersion represented using calculated Boussinesq distribution  
 $f_m$  = masonry compressive strength

A breakdown of the estimated time requirements is given in Table 9. The time values are scaled for a person acquainted with FEM modelling but not a regular user. It is assumed that all input parameters have been determined before model preparation begins. This is often the most time-consuming part of the process, but it varies significantly over different projects, due to different project constraints and availability of field test data.

FEM model preparation is always a time-consuming process due to the inherent complexities of defining geometry, material models, meshing, etc. However, imperfect familiarity with the modelling program significantly adds to the time. The user guide must frequently be consulted to define the more complex parameters, and the process itself becomes iterative as previous steps must be modified or corrected. Advanced users will be able to speed up this process significantly. However, the same modelling efficiency as RING will never be obtained, as users familiar with RING can build a model in less than 5 minutes.



Interpretation of FEM results takes time because usually multiple models must be run and compared before any conclusions can be drawn. Oftentimes convergence issues develop, requiring refinement of the input parameters. RING, on the other hand, only gives a few critical output parameters, and these are relatively easy to interpret. For all of these reasons, RING is by far the fastest and simplest modelling approach.

Table 9: Estimated time requirements

Program	Time (hours)			
	Model preparation	Analysis	Interpretation	Total
RING	1.0	< 10 sec	1.0	2.0
ATENA	16.0	1.5	8.0	25.5
ADINA	16.0	0.1	8.0	24.1

Table 9 shows that the FEM time requirements are an order of magnitude higher than the RING time requirements. The time required for analysis is also important, even though the values are relatively small. For the RING and ADINA models, many variations could easily be run, quickly troubleshooting problems or testing simple hypotheses. The ATENA model, on the other hand, used the smeared crack model, and thus required many iterations on each step before convergence was reached. These results show that for the case study used the RING model is the most time-effective, and given that very little sacrifice is required in terms of load-carrying capacity, it should be used in most situations.

This page intentionally left blank.

## 9 CONCLUSIONS

This study analyzed a two-span masonry arch bridge using several different analysis techniques. Limit analysis “by hand”, assuming no tensile strength and infinite compressive strength, and incorporating only the vertical load effect of the infill, gave a load factor of 4.02. This method is automated and improved on in the rigid-block analysis program RING, allowing for load dispersion, passive horizontal infill restraint, and compressive crushing. Using this program, a load factor of 11.5 was obtained. Two FEM models were also built, using the smeared crack and discrete crack models respectively. Some simplifying assumptions were used, including modelling in 2D, isotropic idealization of masonry, and elastic-perfectly-plastic response in compression. The smeared crack model failed to converge at a load factor of 13.2, while the discrete crack model failed to converge at a load factor of 13.5. Failure occurred in the infill before the load capacity of the arch itself could be obtained. It was hypothesized that the failure in the infill was the result of modelling assumptions, and did not correspond to a structural failure state. For this reason, a model was built in which the load was applied directly to the arch extrados using a Boussinesq distribution. The discrete crack model was also used for this test. With these assumptions, a load factor of 21.8 was attained. More study is needed to determine whether or not failure in the FEM infill model can safely be neglected. If it can be neglected, this result gives the estimated load capacity of the arch itself, and shows that a Boussinesq load distribution on the arch extrados can be used to model arch failure.

The rigid-block analysis using RING was able to achieve almost the same load capacity as the FEM models with load applied on top of the infill. RING is very labor- and computationally-efficient, as a RING model can be built and run in less than an hour, while FEM models may require days of work. This strongly suggests that in most cases, the additional work required in creating FEM models is likely not warranted. If, however, an FEM model is created with the purpose of achieving a higher estimated load capacity, it is advised that the model should use more detailed modelling assumptions than those used in this analysis program. Specifically, improvements could include:

- Modelling in 3 dimensions.
- Using a masonry material that accounts for anisotropy.
- Including a slip plane between the arch extrados and infill elements.
- Modelling of the road surface and base fill to better distribute live loads, decreasing the point load effect on the low-stiffness infill.

While it requires more time and effort, FEM modelling provides information on intermediate loading states that cannot be obtained in RING. This information can be particularly useful in specifying service-level load ratings. In this study, a historic load rating criterion requiring 67% of the critical section to be in compression was compared with a suggested criterion taking the service load as the first initiation of the fourth hinge. The load factor corresponding to the fourth hinge initiation is 1.8 to 2.4 times higher than that corresponding to 67% compression. Furthermore, the maximum load attained was more than double that observed at fourth hinge initiation for all cases. This indicates that failure propagates over a wide range of loading values, meaning the lower service-level limits may be used with a high level of confidence. Using the fourth hinge initiation criterion with a dynamic loading reduction factor, a load rating of 5.0 was calculated.

RING was also used to compare various loading patterns and infill modelling techniques. The effects of load dispersion and load placement (centered or off-center) were found to be small. On the other hand, the horizontal passive pressure effect of the infill is quite large, more than tripling the estimated load capacity. Thus, analysis techniques that do not consider this effect will be conservative. Also, since the effect is so large, care should be taken when selecting the strength parameters of the infill.

## 10 REFERENCES

- American Association of State Highway Officials, 2012. *AASHTO LRFD Bridge Design Specifications*. 6th ed. Washington, D.C.: AASHTO.
- Atamturktur, S., Ross, B., Thompson, J. & Biggs, D., 2016. Compressive strength of dry-stacked concrete masonry unit assemblies. *Journal of Materials in Civil Engineering*.
- Audenaert, A., Reniers, G., Dullaert, W. & Peremans, H., 2009. Evaluation of the limit load capacity of masonry arch bridges. *WSEAS transactions on applied and theoretical mechanics*, 4(4), pp. 137-146.
- Biggs, D. & Rogers, H., 1987. *Rehabilitation of an historic stone masonry bridge*. Troy, NY, IBC.
- Block, P., DeJong, M. & Ochsendorf, J., 2006. As hangs the flexible line: Equilibrium of masonry arches. *Nexus Network Journal*, 8(2), pp. 13-24.
- Boothby, T. & Fanning, P., 2004. Load rating of masonry arch bridges: Refinements. *Journal of Bridge Engineering*, Volume 9, pp. 304-307.
- Borri, A., Corradi, M., Castori, G. & De Maria, A., 2014. A method for the analysis and classification of historic masonry. *Bulletin of Earthquake Engineering*, Volume 13, pp. 2647-2665.
- Borst, R. d., Remmers, J., Needleman, A. & Abellan, A., 2004. Discrete vs smeared crack models for concrete fracture: Bridging the gap. *International Journal for Numerical and Analytical Methods in Geomechanics*, Volume 28, pp. 583-607.
- Cavicchi, A. & Gambarotta, L., 2007. Lower bound limit analysis of masonry bridges including arch-fill interaction. *Engineering Structures*, Volume 29, pp. 3002-3014.
- Heyman, J., 1982. *The Masonry Arch*. Chichester: John Wiley & Sons.

IMIT Circ. 02.02.2009, n. 617:, 2009. *Istruzione per l'applicazione delle Nuove Norme Tecniche per le Costruzioni di cui al decreto ministeriale 14 gennaio 2008*, Rome, Italy: Italian Ministry of Infrastructure and Transportation.

Institute of Civil Engineers, 2008. *ICE Manual of Bridge Engineering: Second Edition*. London, UK: Thomas Telford, Ltd.

Jaafar, M. et al., 2005. Strength correlation between individual block, prism and basic wall panel for load bearing interlocking mortarless hollow block masonry. *Construction and Building Materials*, Volume 20, pp. 492-498.

Kidder, F., 1905. *The architect's and builder's pocket-book*. 14th ed. New York: John Wiley & Sons.

LimitState Ltd, 2016. *LimitState:RING Manual*, Sheffield, UK: s.n.

Loo, Y. & Yang, Y., 1991. Cracking and failure analysis of masonry arch bridges. *Journal of structural engineering*, 117(6), pp. 1641-1659.

Lourenço, P., 1996. *Computational strategies for masonry structures*, Delft: Doctoral dissertation, Delft University of Technology.

Lourenço, P., 2010. Recent advances in masonry modelling: Micromodelling and homogenisation. In: U. Galvanetto & M. Aliabadi, eds. *Multiscale Modelling in Solid Mechanics: Computational Approaches*. London, UK: Imperial College Press, pp. 251-333.

Lourenço, P., Almeida, J. & Barros, J., 2005. *Experimental investigation of bricks under uniaxial tensile testing*, s.l.: British Masonry Society.

Magenes, G., Penna, A., Galasco, A. & Rota, M., 2010. *Experimental characterisation of stone masonry mechanical properties*. Dresden, International Masonry Society.

Page, J., 1987. *Load tests to collapse on two arch bridges at Preston, Shropshire and Prestwood, Staffordshire*, Crowthorne, England: Department of Transport.

Pippard, A., 1936. The mechanics of the voussoir arch. *Journal of the Institute of Civil Engineers*, Volume 4, pp. 281-306.

Roca, P., Cervera, M., Gariup, G. & Pela, L., 2010. Structural analysis of masonry historical constructions. Classical and advanced approaches. *Archives of Computational Methods in Engineering*, Volume 17, pp. 299-325.

van der Pluijm, R., 1999. *Out-of-plane bending of masonry: behaviour and strength*, The Netherlands: Eindhoven University of Technology.

Vasconcelos, G., 2005. *Experimental investigations on the mechanics of stone masonry: Characterization of granites and behaviour of ancient masonry shear walls*, Guimaraes, Portugal: University of Minho.

www.geotechdata.info, 2013. *Soil Elastic Young's Modulus*. [Online] Available at: <http://www.geotechdata.info/parameter/soil-young%27s-modulus.html> [Accessed 06 06 2017].